Master thesis and internship[BR]- Master's thesis : LQG controller development for active isolation of future gravitational wave detectors from low-frequency seismic motion[BR]- Integration Internship

Auteur : Thibaut, Brieux
Promoteur(s) : Collette, Christophe
Faculté : Faculté des Sciences appliquées
Diplôme : Master en ingénieur civil en aérospatiale, à finalité spécialisée en "aerospace engineering"
Année académique : 2021-2022
URI/URL : http://hdl.handle.net/2268.2/14374

University of Liège - Faculty of applied sciences

LQG controller development for active isolation of future gravitational wave detectors from low-frequency seismic motion

Promotor

Colette Christophe

Author

Thibaut Brieux

Graduation Studies conducted for obtaining the Master's degree in Aerospace Engineering by Brieux Thibaut

Academic year 2021 – 2022

Acknowledgements

I would first like to thank Professor Christophe Colette, my promoter, for his expertise as well as the whole team of PhD students who followed me throughout the process. They were available to discuss my work when I needed them and to give me constructive feedback.

I am particularly grateful to Haidar Lakkis who, during our exchanges, provided me with answers to my questions and gave me wise advice. Without him and his availability, this thesis would not have been possible.

Finally, I also thank my family and friends for their support. A special thanks to Lola for her proofreading and encouragement during the elaboration of this work.

Brieux Thibaut

Abstract

The mysteries of the universe have always fascinated people on earth. Hence, methods to observe and study it in details have been and are still being developed. Since the first detection of gravitational wave at LIGO (Laser Interferometer Gravitational-wave Observatory) in 2015, a new tool to study the universe was added to the panel of existing ones. It is called gravitational wave astronomy.

However, the detection of such waves is a technical challenge as their effects are extremely small. As a result, the detectors that aim to capture them must have a tremendous degree of precision. The various noise sources to which they are subjected must then be drastically reduced. An important one is the vibration of the detector due to seismic motion. Passive as well as active isolation systems are thus employed to isolate the detector from the ground motion.

The goal of this work is to design a type of optimal controller called linear quadratic Gaussian controller on an existing experimental isolation platform. The design is separated into two main steps. The first is the development of a full-state observer to estimate the states of the isolation platform from its outputs. The second is the design of a linear quadratic regulator to control the system. The two are then combined to form the complete controller to be used as feedback in a closed-loop system with the initial plant.

The performances of this controller are finally analysed and discussed. From this analysis, it emerged that the controller allows to increase the isolation performances of the platform by about one order of magnitude between 0.1 Hz and 1 Hz and by two order of magnitudes from 1 Hz to 10 Hz. Therefore, conclusion has been made that this type of controller were appropriate to provide good isolation performances to the experimental platform in the control bandwidth $[0.1, 10]$ Hz. The next step is now to implement it experimentally to address its performances in real situations.

Contents

1 Introduction

Since the dawn of time, men have been looking up to the sky and wondering what it was made of. It began as a philosophical opinion in ancient times and elaborated into scientific studies by observing the movement of the visible stars and planets in the sky. The visible light was the only way to observe the universe around the Earth for most part of humanity. It is not until recently, over the last century, that new technologies have made it possible to observe the sky in the whole range of the electromagnetic spectrum or through particle detectors. Nowadays, many instruments, each exploiting a particular wavelength range from gamma rays to radio waves, continuously scan the sky to unravel its mysteries. They picture the world in their own way and complement each other. In an effort to understand the world in its smallest details, people are always looking for new ways to observe the universe and new technologies to make existing ones more efficient and accurate.

In 2015, the detection at LIGO (Laser Interferometer Gravitational-wave Observatory) of gravitational waves (G.W.) produced by the merger of two super massive black holes was a breakthrough in the field of observational cosmology. Two important outcomes emerged from this discovery. On the one hand, it supports Einstein's theory of general relativity on which many actual theories and applications of physics are based. And on the other, it gives mankind a whole new tool for studying the universe, through gravitational wave astronomy.

1.1 Gravitational waves

To understand the concept of gravitational waves, the concept of gravity and space-time as laid out in Einstein's general relativity theory must first be understood. In this theory, the three dimensions of space and the single dimension of time are not distinct from each other, as opposed to the classical theory of gravity proposed by Newton. Indeed, they interact with each other to form the four-dimensional space-time continuum conception of the universe. Moreover, this space-time is no longer flat nor immutable. Instead, it is distorted by the presence of matter and energy as illustrated in Fig. 1 [1].

This new conception of the universe was motivated by the direct contradiction between the instantaneousness of the gravitational force in Newton's theory and his freshly released special relativity theory. Indeed, in the latter, the speed of light in a vacuum is a finite invariant and is considered the maximum speed at which information can travel through space [3]. In his theory of general relativity, Einstein gets around this problem by proposing that gravity is no longer an instantaneous force acting between massive bodies. Instead, he suggests that it is the consequence of the curvature of space-time. Gravity is then seen as a dynamic field in which bodies are immersed and which dictates the

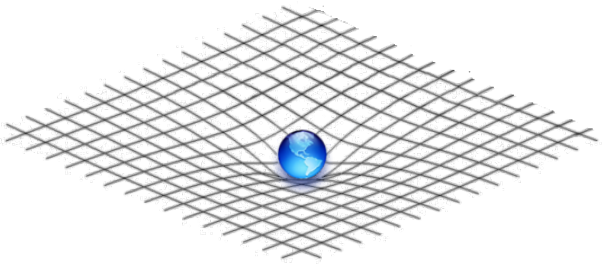

Figure 1: 2D schematic view of the deformation of the space-time continuum induced by the presence of a massive body. Retrived from [2].

motion of matter and energy. This new formalism has solved several problems encountered by Newton's theory, one being the instantaneous nature of the gravitational force [1].

The motion of massive bodies through space-time affects its curvature. Hence, its geometry is in constant evolution. However, as mentioned earlier, the evolution of space-time curvature cannot be instantaneous to be consistent with Einstein's relativity theory. The theory therefore predicts that the information travels at the speed of light, which is finite, in the form of waves called gravitational waves [1]. Any accelerating mass creates gravitational waves whether it is a person, a plane, or a star. However, the principal sources, i.e. those creating waves of highest amplitudes and energy, are either single spinning massive objects, compact binaries made of two massive objects, the merger of two massive objects or supernovae core collapse. The two massive objects mentioned are essentially black holes or neutron stars [4].

When a gravitational wave passes through an object, it distorts the body in the transverse plane to the direction of propagation. Its effects are illustrated schematically in Fig. 2 for an initially circular ring of particles spanned by a gravitational wave propagating in the $\hat{z}$ direction. The wave induces alternative contractions and elongations along the $\hat{x}$ and $\hat{y}$ directions for its first polarization, noted $+$, and along the $\hat{y} = \hat{x}$ and $\hat{y} = -\hat{x}$ directions for the its second polarization, noted $\times$.
The effect of gravitational waves is however extremely small. Indeed, for an initial ring size L_0, the length variation due to the gravitational wave amounts to

$$\delta L \sim \frac{1}{2} h L_0 \tag{1}$$

where the typical strain amplitude of gravitational waves from astrophysical sources is $h \lesssim 10^{-21}$. Thus for a body of 1 km in length, it constitutes a maximum variation of 10^{-18} m [5]. The observation of gravitational waves is therefore a technical challenge and, as of today, only tremendous events can be detected.

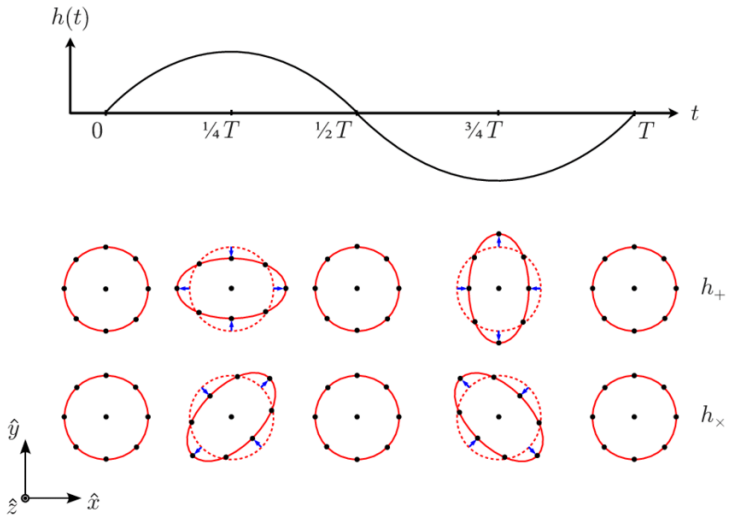

Figure 2: A monochromatic gravitational wave of pulsation $w = 2\pi/T$ propagating along the $\hat{z}$ direction. The lower panel shows the effects of the + and × polarizations on a ring of freely falling particles, in a local inertial frame. Retrieved from [5].

1.2 Gravitational wave detectors

There are three main possible methods for detecting and studying gravitational waves. They will be listed in order of increasing detection frequency range. The first method is to study the cosmic microwave background polarization to learn about the gravitational waves emitted in the early moments of the universe [6]. These G.W. have been estimated to have a very low frequency spectrum in the range of $[10^{-18}, 10^{-16}]$ Hz [7]. The second is to use pulsar timing arrays (PTA). A pulsar is an astronomical object that produces a periodic signal ranging from milliseconds to tens of seconds. For instance, a neutron star rotating very rapidly on itself and emitting strong electromagnetic radiation in the direction of its magnetic axis. A PTA is a collection of pulsars that are continuously monitored by various ground-based radio telescopes to record the time of arrival (ToA) of the pulses they emit. Gravitational waves cause their ToA and thus their frequency to vary. These variations are then collected on Earth and studied. This technique have a sensitivity in the range of $[10^{-9}, 10^{-6}]$ Hz [8]. The last one is performed using an optical interferometer which can either be ground-based or space-based. The detection range is, with the current technology, around $[10^{-4}, 10^{4}]$ Hz [9]. This is the technique of interest for this thesis and is detailed hereafter. The gravitational wave frequency spectrum as well as the range at which each type of detector is effective is shown in Fig. 3.

To detect the extremely small distance variations caused by gravitational waves, an optical interferometry technique based on the Michelson interferometer is used. The basic principles of the latter are explained in the following and illustrated in Fig. 4.

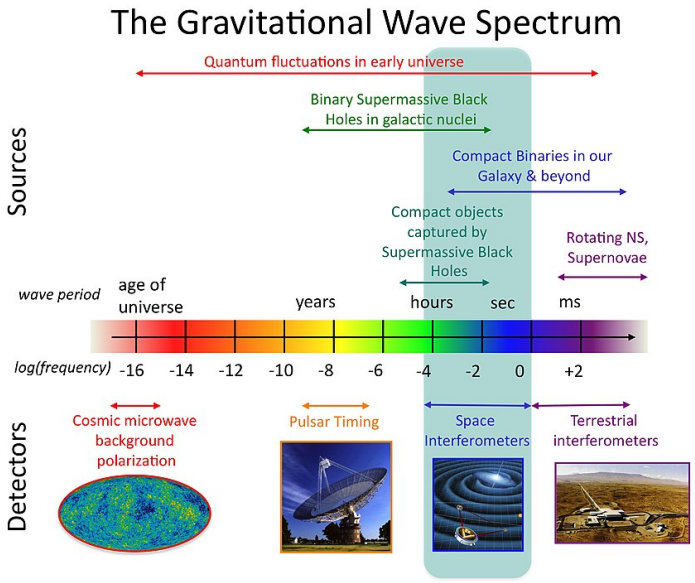

Figure 3: The spectrum of gravitational waves with possible sources and detectors. Retrieved from [9].

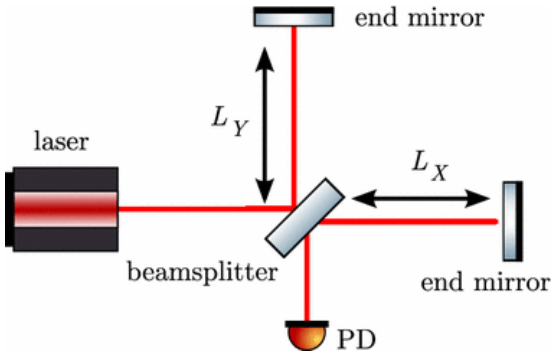

Figure 4: Simplified layout of a Michelson interferometer. Retrieved from [10].

The detector basically consists of two mirrors, a beam splitter, a light source, and a photodetector. The light source, typically a laser, emits a beam of light that, after passing through the beam splitter, is split into two separate beams travelling in perpendicular directions towards each mirror. After reflection, they recombine at the beam splitter and produce an interference pattern incident on the photodetector. Under normal conditions, the detector detects a beam of constant intensity dependent on the differential path length between the two arms ($\Delta L = L_X - L_Y$). But when a G.W. passes through, the detector's arms undergo length variations that produces a characteristic interference captured by the photodetector [11]. This signal is then analysed and studied to understand what it can reveal about its origin.

1.3 Noises

Since the strain produced by gravitational waves to be detected are extremely small, the question of induced noise on the detector arises. If the order of magnitude of the noise is greater than that of the signal, then the detection is hopeless. A significant part of the work of detecting gravitational wave is the assessment and reduction of all types of noise hindering the measurements. There are numerous noise sources, the main ones being photon shot noise, radiation pressure noise, the standard quantum limit, thermal noise, and seismic noise. This thesis is particularly focused on seismic noise isolation, therefore, only this type of noise will be addressed in details. Further discussion about the other types of noise can be found in [12].

Seismic noise acts on the interferometer via two main channels. First, seismic excitation can mechanically couple to the detector's structure. Second, it can excite density fluctuations in the environment of the detector which couple to the test mass position through gravitational attraction. This one is commonly called Newtonian noise. It is well known that the ground is constantly in motion due to seismic activity on the one hand, and human activity on the other. This greatly affects ground-based G.W. detectors as the ground motion exceeds the expected differential displacement between the test masses due to G.W. effects by several orders of magnitude. For example, the ground motion measured at the location of Virgo, A G.W. detector in Italy, reaches up to $10^{-9}\mathrm{m}/\sqrt{\mathrm{Hz}}$ at 10 Hz. If a detector was to detect gravitational waves with a strain of $h \simeq 10^{-22}$, it should achieve a sensitivity at least as good. For a 1 km arm's length detector, a strain sensitivity of $h \simeq 10^{-22}$ corresponds to a differential displacement of $\Delta l \simeq 10^{-19}\mathrm{m}/\sqrt{\mathrm{Hz}}$. Thus, in order to reach this sensitivity and capture the G.W. signal, the seismic motion must be suppressed by a factor of 10^{10} [12]. The methods for controlling the ground motion to reach the sensitivity desired for G.W. detection will be the main focus of this thesis.

1.4 Motivations

Current ground-based G.W. detectors have a strain sensitivity limited to the order of $10^{-23}/\sqrt{\mathrm{Hz}}$ with a frequency bandwidth of detection of $[10, 10^4]$ Hz [12]. With these specifications, the sources of G.W. events that can be detected are very limited. Only the most violent and closest to Earth can be observed as the G.W. fade away as they travel through space. This is the reason why it is important to increase the sensitivity of the detectors to detect smaller and further away events. An attempt to increase the sensitivity of existing detectors has already been done but this improvement is limited by their available infrastructure and only small improvements can be achieved. To make significant sensitivity improvements compared to advanced detectors, new facilities with

novel technologies must be built.
As it will be seen in Sec. 2.1, today's detectors are very limited at low frequencies, below 10 Hz, due to seismic and Newtonian noises. There is therefore a need to develop more efficient isolation systems. An important part of active isolation systems development is the design of the control strategy. The controller links the sensors to the actuators. It reads the information coming from the sensors and uses them to dictate the action of the actuators. It has to be done in the most efficient way to isolate the payload as well as possible. This thesis is focused on the controller design part of isolation systems. There are many types of controller with their advantages and drawbacks. Here, a Linear Quadratic Gaussian (LQG) regulator is developed for an existing passive-active isolation system targeting the [0.1, 10] Hz frequency bandwidth.

1.5 Thesis outline

This works starts with a review of the existing gravitational wave detectors with their isolation method against seismic motion as well as their achieved sensitivity, see Section 2. Then, the principle of passive and active isolation are laid out. Section 3 focuses on the basics of the control theory. The linear quadratic regulator (LQR), the Kalman filter, and the linear quadratic Gaussian controller are discussed. Next, in Section 4, the components of the experimental isolation platform, for which the controller is designed, are presented. Section 5 contains the details of the LQG controller development. Its performances are then analysed in Section 6. Finally, Section 7 will conclude this work and present some perspectives for improvement.

2 State of the art

This section presents a review of the literature concerning gravitational wave detectors as well as current methods of vibration isolation.

2.1 Gravitational wave detectors

There are four main ground-based gravitational wave detectors based on interferometry currently in operation. They are part of a worldwide network of second generation detectors joining forces in the quest for gravitational waves. Having a network of detectors is crucial for two reasons [12]. The first is for coincidence of detection. Measuring a gravitational wave simultaneously at several distant locations increases the confidence that the signal comes from extraterrestrial source rather than technical glitches in the detector outputs. The second is for sky localisation. In order to locate the position in the sky of the G.W. source, a triangulation method is used based on the arrival times at the various detectors. The more the detectors and the further away they are from each other, the better is the accuracy of the localisation. Each detector has particular features and different strain-sensitivity curves. An additional one is currently under study in order to increase the sensitivity and detection bandwidth. It will be the first of third generation detectors and is called the Einstein Telescope.

Moreover, space-based laser interferometers for G.W. detection are being thought of. Many mission proposals have been put forward with the main one being the Laser Interferometer Space Antenna (LISA)[13]. Space-based detectors are not submitted to the same noise sources than those on Earth which allows them to reach a good sensitivity at much lower frequencies. They can thus be complementary with the ones on Earth. In the following, the sensitivity of each detector will be briefly discussed as well as the isolation methods employed against seismic noise.

2.1.1 Advanced Virgo

The Advanced Virgo is the upgrade of the first generation Virgo detector situated 15 km southeast of Pisa in Italy. It is therefore said to be a second generation detector.

The Virgo isolation technique is essentially based on an hybrid (passive–active) attenuation system called the *Superattenuator* (SA), viewed in Fig. 5, to which each mirror of the interferometer are attached [14]. It is composed of a five-stage pendulum supported by a three-leg elastic structure called *Inverted Pendulum*. It makes a chain of mechanical filters for which the transmitted horizontal displacement of the suspension point is decreased

at each stage. In an N-stage pendulum, the displacement transmitted to the last stage, at a frequency f higher than its normal modes, is reduced by a factor proportional to f^{2N}. The pendulum chain has been designed to confine all the normal modes below 2 Hz, in order to have an attenuation of the ground horizontal seismic noise by more than 10 orders of magnitude, starting from a few Hz.

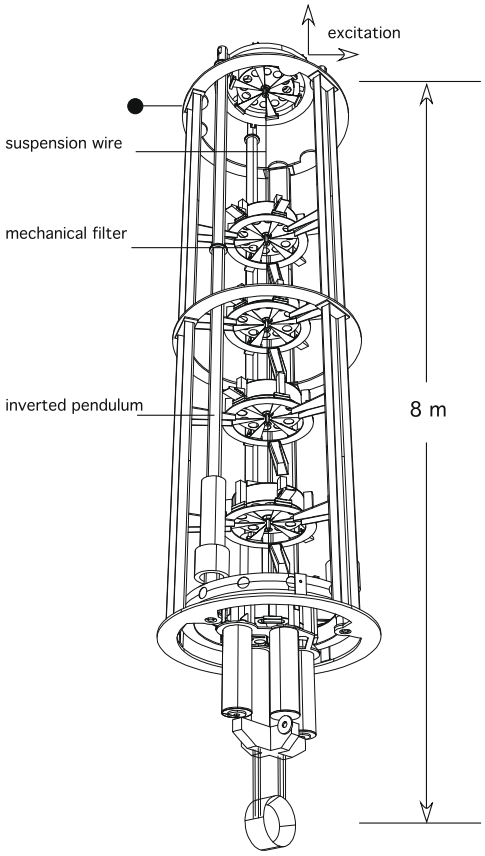

Figure 5: Schematic view of the Virgo *Superattenuator*. Retrieved from [14].

Regarding the seismic vibration in the vertical direction, the multi-stage pendulum includes cylindrical mechanical filters with a set of concentric cantilever blade springs with low stiffness. They are connected through an about one meter long steel wire forming a chain of low frequency oscillators in the vertical direction. They work in parallel with a magnetic anti-spring system to reduce its fundamental vertical frequency. This assembly reduces all the vertical modes of the chain below 2 Hz and thus isolates well the mirror from the vertical seismic noise above a few Hz. However, between 200 mHz and 2 Hz, the seismic excitation is amplified by the normal modes of the filter chain. This drives a high amplitude swinging motion of the mirror (> 10 μm) which is not acceptable for keeping the cavities at resonance (an accuracy of $10^{-12} - 10^{-10}$ m in the mirror positioning is necessary). This displacement must therefore be actively controlled to maintain the interferometer in the working position. To this end, an inertial control system (Inertial Damping), acting on the suspension top stage, is employed. For longitudinal direction

isolation, it is based on the association of three high sensitivity accelerometers and three coil-magnet actuators. The accelerometers monitor the suspension point acceleration in the horizontal plane (two translations and one rotation about the vertical axis) and the three actuators are used in feedback to keep the position of the top stage locked to an inertial frame. Damping of the vertical resonances is achieved in a similar way with two accelerometers and two coil-magnet actuators used in feedback. The considerable ultra-low frequency mirror displacements (hundreds of microns below 10 mHz) are compensated using the interferometer as sensor and the three coil-magnet pairs of the horizontal Inertial Damping as feedback actuators. The overall system is capable of reducing seismic noise by more than 10 orders of magnitude in all six degrees of freedom (dof) above a few Hz.

Since the SA performance already met the sensitivity requirement of AdV, no major changes have been brought to it. Though, a new design of the payload has been developed in order to be able to suspend heavier mirrors [15]. Moreover, an upgraded controller design has been developed and an active system to control the ground tilt has been implemented. In Virgo, classical Nyquist-like techniques were used in order to diagonalize the multiple-input multiple-output (MIMO) system to obtain a set of single-input single-output (SISO) systems. The upgraded detector now makes use of a multivariable design approach based on optimal predictive regulators. This has the advantage to be an automatic and optimal process which allows to optimize the feedback performance for both the mixed and diagonal term elements of the sensor/actuator transfer function matrix. During earthquakes or bad weather conditions, seismic motion can be drastically increased in the $[0.1, 1]$ Hz band. Its angular component fully transmitted to the SA can, as a result, reach high enough levels to compromise the duty cycle of the interferometer optical configuration. To prevent this from happening, a set of piezo-electric actuators coupled with sensors providing tilt measurements uncontaminated by translational components are used in closed-loop As a result, thanks to the suspension chain, the seismic noise is attenuated by 14 orders of magnitude above 10 Hz. The longitudinal and angular motion control strategies are detailed in [16].

A graph representing the strain-sensitivity curve of Virgo and the target sensitivity of advanced Virgo as a function of the frequency can be seen in Fig. 6. The initial Virgo detector had achieved a sensitivity of $5 \cdot 10^{-23}/\sqrt{\text{Hz}}$ around 100 Hz and of $10^{-21}/\sqrt{\text{Hz}}$ in the $[20, 1000]$ Hz bandwidth [17]. The advanced Virgo was designed to achieve a sensitivity of one order of magnitude better and was successfully. It corresponds to a substantial increase in the detection rate by about three orders of magnitude.

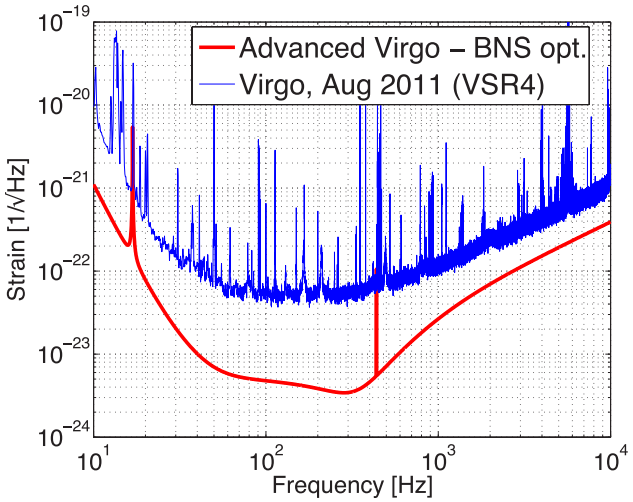

Figure 6: The Virgo strain-sensitivity as a function of frequency compared to the Advanced Virgo target. Retrieved from [18].

2.1.2 Advanced LIGO

The advanced LIGO is the upgrade of the first generation LIGO (Laser Interferometer Gravitational-Wave Observatory). It operates two gravitational wave detectors in the USA, one situated near Livingston, Louisiana, and the other near Hanford, Washington. Moreover a collaborative project between a consortium of Indian research institutions and the LIGO Laboratory is envisaged [19]. The project is to build an additional LIGO detector, called LIGO-India, in India to expand its network.

As Virgo, the LIGO detector profits from passive-active isolation platforms to isolate the payload from seismic noise [20]. Figure 7 shows the seismic isolation platforms used for the auxiliary optics and for the core optics. The former is called the Horizontal Access Modules (HAM) and the latter the Basic Symmetric Chambers (BSC). They each feature a pre-isolation stage externally to the vacuum chamber containing the payloads. It is called Hydraulic External Pre-Isolator platforms (HEPIs) and provides one stage of active isolation. Then, for the isolation of auxiliary optics, a single-stage Internal Seismic Isolators (ISI) mounted on the HEPI inside the vacuum chamber (HAM-ISI) is used. This adds one stage of passive-active isolation. Finally, the auxiliary optics components are suspended by up to the three stages of passive suspensions, inspired by GEO600 suspensions. As for the isolation of the more critical core optics, two-stage seismic isolators mounted on the HEPI (BSC-ISI) are used. They add two stages of passive-active isolation. At last, the core optics are mounted on the down-facing BSC-ISI optical table and are suspended at the last stage of quadruple pendulum suspension.

A graph representing the strain-sensitivity curve of LIGO and the target sensitivity of

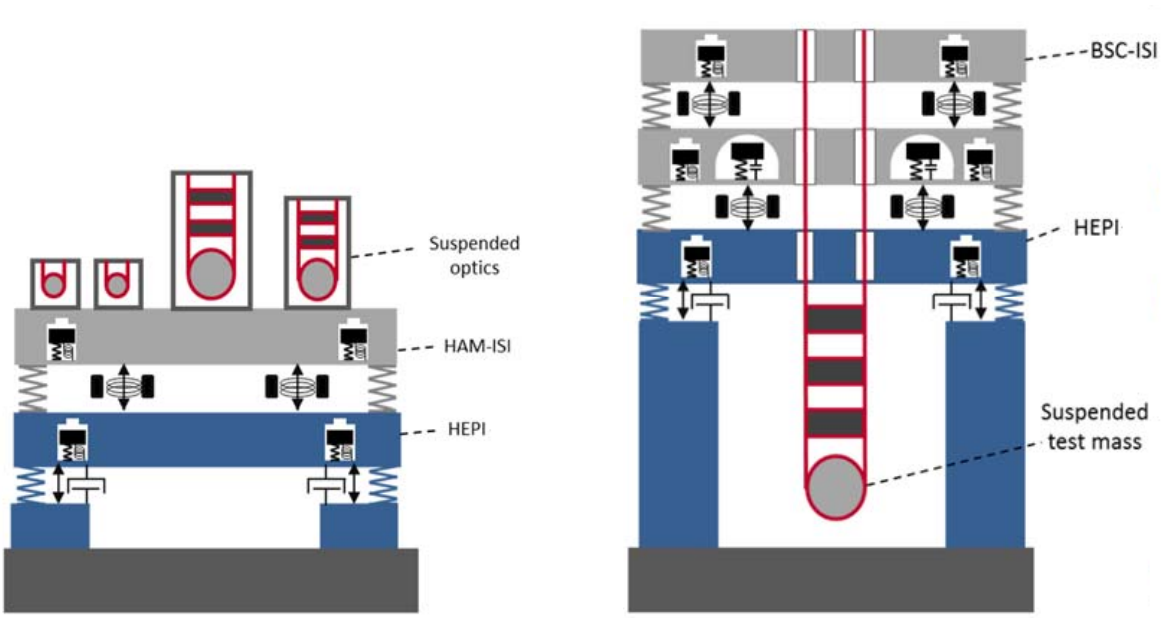

(a) HAM chamber (b) BSC chamber

Figure 7: Schematic view of the passive-active isolation systems of LIGO. a) represents the Horizontal Access module chamber responsible for isolating the auxiliary optics from ground motion. b) represents the Basic Symmetric Chamber responsible for isolating the core optics from ground motion Retrieved from [20]

advanced LIGO as a function of the frequency can be seen in Fig. 8. As the Virgo detector, the initial LIGO had reached a sensitivity of the order of $10^{-23}/\sqrt{\text{Hz}}$ around 100 Hz [18]. Its upgrade (Advanced LIGO) presents a similar target strain-sensitivity curve as Advanced Virgo, cfr Fig. 6, with a little improvement especially at low frequency. The design sensitivity of $2 \cdot 10^{-23}$ around 200 Hz was eventually reached by the 4 km detectors [12]. This sensitivity achieved at LIGO allowed the first ever detection of a gravitational wave signal in 2015.

2.1.3 GEO600

GEO600 is a smaller detector with arm lengths of 600 m located south of Hanover in Germany. It doesn't have as good performances as the bigger ones mainly caused by a significantly limited budget. It thus often tried to compensate this issue with the implementation of novel techniques that were risky and not extensively tested. In this way, it serves as a kind of test bed for new technologies from which advanced detectors can benefit later on. Though, it actually achieved fairly good sensitivities as the new technologies has been successfully implemented.

Concerning the seismic motion isolation of the payload, GEO600 employs a multiple-stage suspensions as Virgo has already been using. However, it integrated the design of multiple-

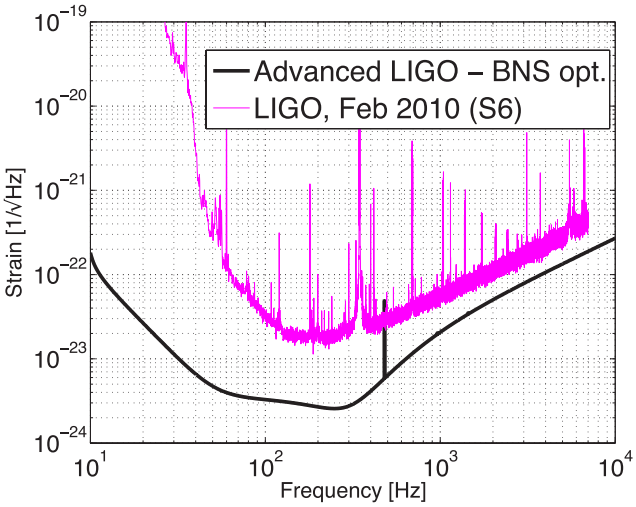

Figure 8: The LIGO strain-sensitivity as a function of frequency compared to the Advanced LIGO target. retrieved from [18].

stage suspensions with a monolithic last stage, electrostatic actuators and a reaction chain that has been the precursor of very similar suspension in advanced LIGO. Further details about these systems can be found in [21]. It also has benefited from an upgrade during the last decade, called GEO-HF, principally aimed at improving the detector's sensitivity at high frequency (> 500 Hz). Since the shot noise was the limiting parameter at high frequencies, a series of improvements, described in [22], seeking to lower it have been implemented. Improvement by up to a factor of 4 of shot-noise-limited sensitivity has been achieved. For lower frequencies (below 500 Hz), the limiting parameter is thermal noises, mainly thermo-refractive noise at the beam splitter and coating Brownian noise. Reduction of these noise sources were not investigated as it was not the goal of this upgrade [23].

A graph representing the target strain-sensitivity curve of GE0600-HF compared to the sensitivity curves after completion of significant upgrades to the initial GEO600 can be seen in Fig. 9. In addition, the major noise sources and the sensitivity of the VIRGO S6e science run from 2010 are also depicted. From this, it can be seen that the targeted frequency bandwidth is $[10^2, 10^4]$ Hz with a sensitivity around 10^{-22}. Also, the limiting noise of GEO-HF is thermal noise at low frequency and shot noise at high frequency.

2.1.4 KAGRA

The latest kilometer-scale detector built is the 3 km Japanese Kamioka Gravitational Wave Detector (KAGRA). It has implemented two major technologies valuable for the next generation of detectors. The first is to build the entire facility completely underground to reduce seismic and Newtonian noises. The second is to cool the interferometer's mirrors down to cryogenic temperatures ($< 20\ K$) to decrease the amount of thermal noise

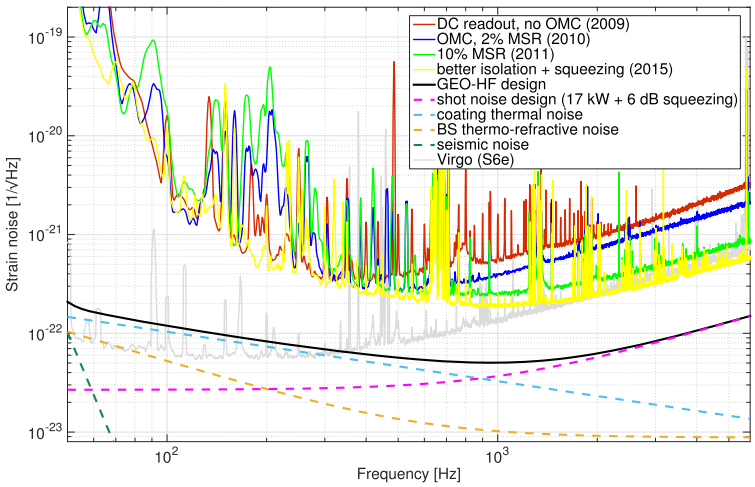

Figure 9: Progression of strain-equivalent noise curves upon completion of major milestones of the GEO-HF upgrade program compared to the GEO-HF design noise curve. Retrieved from [23]

limiting the sensitivity around 100 Hz.

It is built deep underground in the Kamioka mine in Gifu Prefecture, Japan, a seismically quiet site. The wise choice of KAGRA building site has allowed to lower the seismic noise level in the sub-Hz domain for being isolated from anthropological activities as well as above 10 Hz for being built underground [24]. Indeed, at ground level above the detector's location, the level of seismic noise above 10 Hz is raised by a factor of 100 or more in comparison. Moreover, being underground allows to be further away from any anthropological activity which has been the main source of seismic Newtonian noise for detectors built on Earth surface. As a result, this type of noise has been reduced by approximately one order of magnitude above 10 Hz in comparison to LIGO .

Regarding the seismic noise cancellation systems, the detector employs four types of system depending on the residual displacement requirements of each mirror [25]. They are called Type-A, -B, -Bp, and -C systems. The overview of the detector with the type of system used for each optic component is presented in Fig. 10(a). The most critical payloads for G.W. detection are isolated with the type A systems, showed in Fig. 10(b). It will be briefly discussed here but further details about the four system types are given in [26].
The type A isolation system is a 14 m 9-stage pendulum operating inside a vacuum chamber from which is suspended the test mass [26]. The first is a pre-isolator unit made of inverted pendulums (IPs) for horizontal isolation and a geometrical anti-spring (GAS) filter for vertical isolation. The four following stages are equipped with a GAS filter. The first five stages operate at room temperature whereas the last four operate at cryogenic

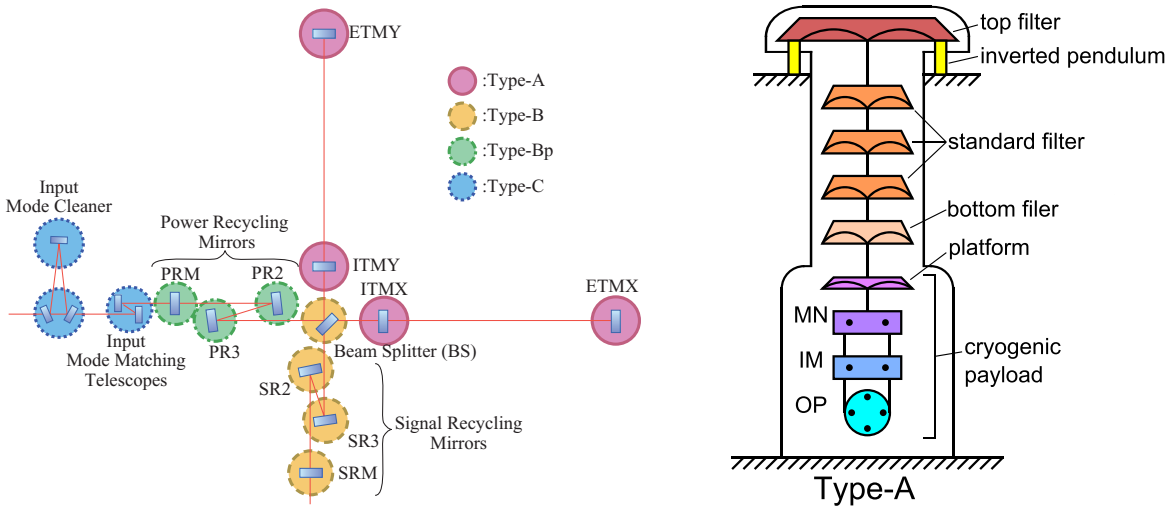

(a) (b)

Figure 10: (a): Schematic of the optical components of KAGRA and the type of vibration isolation system for each of them. ITMX(Y): input test mass X(Y), ETMX(Y): end test mass X(Y). Retrieved from [25]. (b): Schematic of the type A vibration isolation system. MN: marionette, IM: intermediate mass, OP: optic. Black dots represent the location of coil-magnet actuators. Type-A systems are located inside a vacuum tower and the legs of the inverted pendulum table is fixed onto the ground of the second floor. Retrieved from [26]

temperature. The mirror is cooled down to 20 K and the cryogenic payloads are cooled down to 16 K except the sapphire mirror which is only maintained at 20 K because of the heat absorption from the laser beam. Since the resonant frequency of the IP is as low as 80 mHz, it manages to effectively reduce the micro seismic motion that has large amplitude at low frequencies. The seismic attenuation rate achieved by the type-A system has been measured to be below 10^{-5} at 1.7 Hz and of 10^{-21} at 10 Hz for a carefully modeled suspension chain [25].

A graph representing the design strain-sensitivity curve of KAGRA as well as the major noise sources is found in Fig. 11. The predominant limiting parameter above 10 Hz is quantum noise apart from the peaks corresponding to suspension thermal noise. At low frequency (below 6 Hz), seismic noise limits the detector's sensitivity. This detector hasn't yet reached its target sensitivity and is therefore not as effective as Advanced LIGO or Advanced Virgo. Though, comparable sensitivity is expected within the next few years [24].

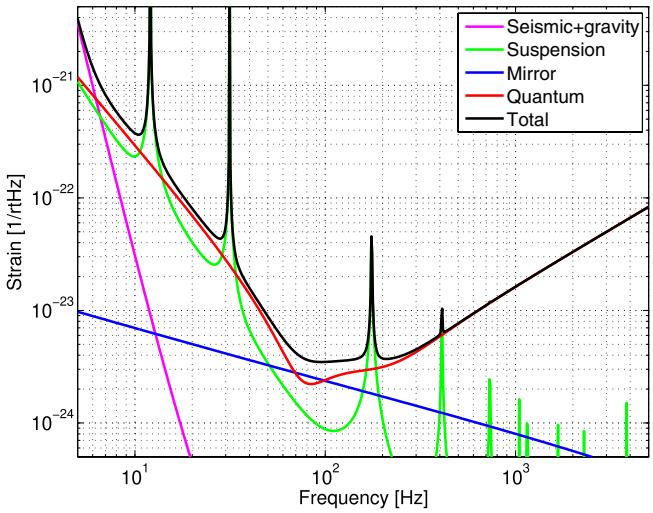

Figure 11: Design sensitivity of the KAGRA detector and the major limiting noise sources. "Suspension" and "mirror" are thermal noises originating respectively from the suspensions and the mirrors. Retrieved from [24].

2.1.5 Einstein Telescope

The Einstein Telescope (ET) is the next generation of gravitational wave detector currently under study. It aims to improve the sensitivity by more than one order of magnitude over second generation advanced detectors and to extend the detection bandwidth in the low frequency range to 1 Hz.

Low frequency sensitivity detectors make it possible to observe intermediate mass black holes (IMBHs), with masses in the range of $[10^3, 10^4]$ solar mass. Moreover, it allows to study coalescing binary systems for a much longer period before their merger. Indeed, they spend long periods at lower frequencies before rapidly chirping up in the final instants. Studying this period would help in measuring the parameters of the source very accurately. Many other scientific potential of ET are discussed in [27].

Although all currently active G.W. detectors are L-shaped since this geometry maximizes the sensitivity with respect to the arm length, ET will be composed of three nested detectors in a triangular shape as shown in Fig. 12. The major drawback is the sensitivity reduction of each detector due to the more acute angle between their arms (60°). However, this is compensated by combining the results obtained at each detector which are complementary [28]. Moreover, a multiple detector facility presents additional advantages in terms of redundancy, signal reconstruction and cost/benefit minimisation [29].

Another innovative concept of ET is to operate two different interferometers in each detector, one optimised for low frequency detection (ET-LF) and the other for high frequency

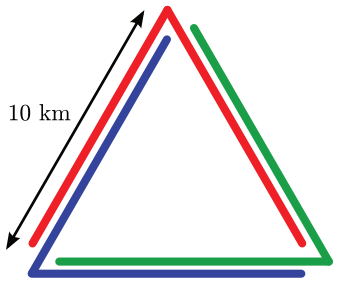

Figure 12: Einstein Telescope triangular configuration with three nested detectors with arms length of 10 km. Retrieved from [12].

detection (ET-HF) [28]. This is the so-called xylophone configuration. This decision was made given the difficulty to increase the sensitivity of both high and low frequencies at the same time. This is a consequence of the different noise sources that come into play at high and low frequencies. For instance, at high frequency, dominant shot noise can be suppressed by high laser power but at the cost of high thermal noise at lower frequencies. In such manner, the xylophone design allows to extend the detection bandwidth by combining the low-frequency-specialised detector and the high-frequency one.

Although seismic noise can be reduced by development of complex isolation systems, the only guaranteed way to reduce the gravity gradient noise is to reduce the initial seismic excitation. Thus, as KAGRA, ET will be built underground to undergo lower seismic activity at its location. Then, the isolation system implemented for the test masses of the interferometer will be an upgraded version of the *Superattenuator* of Virgo [28]. In order to achieve a lower cut-off frequency, the height of the individual pendulum stages of the *Superattenuator* will each be increased by 2 m. The overall modified *Superattenuator* consisting of six pendulum stages (each stage providing horizontal as well as vertical isolation) will attain a height of 17 m.

The strain-sensitivity curves of ET-LF and ET-HF are seen in the two graphs of Fig. 13 along with the principal noise sources affecting them.
At low frequencies, seismic noise limits the sensitivity below 1.7 Hz while gravity gradient noise is dominant between 1.7 and 6 Hz. Above 6 Hz, quantum noise becomes the limiting parameter. The crossover frequency of the two interferometers' sensitivity is around 35 Hz. At higher frequencies, mirror thermal noise limits the sensitivity up to 200 Hz, then quantum noise takes over for the remaining part of the frequency spectrum. If reached, the target design of ET would increase the sensitivity of one order of magnitude at high frequency compared to the second generation of detectors and extend the lower end of the detection bandwidth from 10 Hz to less than 2 Hz [28].

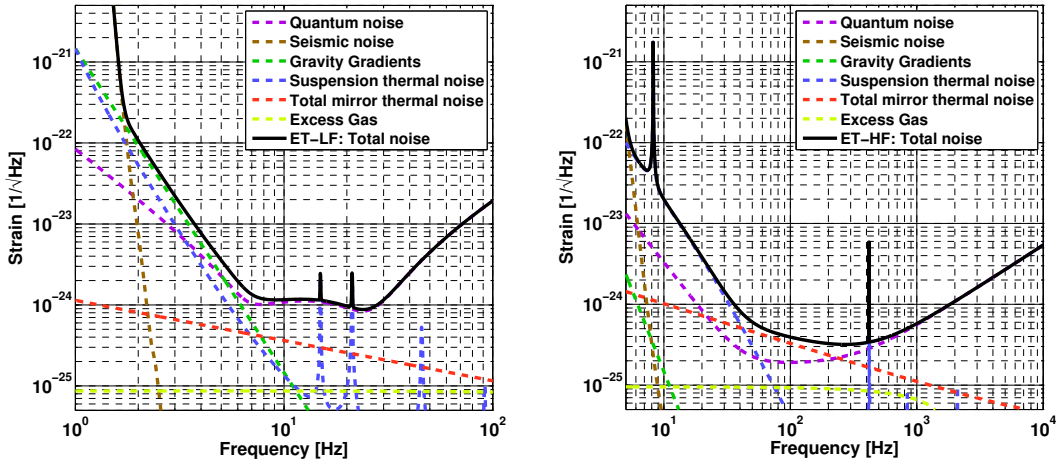

Figure 13: Left: proposed noise budget for Einstein Telescope's low frequency interferometer. Right: proposed noise budget for Einstein Telescope's high frequency interferometer. Retrieved from [28]

2.1.6 LISA

The Laser Interferometer Space Antenna (LISA) is a joint ESA–NASA project to conceive a space-based gravitational wave detector [30]. The reason to develop a space detector is to increase the frequency range of detectable G.W. On the one hand, LISA can avoid noise sources that limit the sensitivity of ground-based detectors at low frequency, and on the other hand, the vastness of space allows an interferometer with extremely long arms which amplify the effect of low frequency gravitational waves. It will be based on the same detection method as the ground-based telescopes i.e. a Michelson interferometer. It will be formed by three spacecrafts in orbit in an approximately equilateral triangle formation with arms of five million kilometres. They will be on an Earth-trailing, heliocentric orbit approximately 20° behind Earth.

The micro-gravity environment of space is naturally suited to freely floating masses. Therefore, there is no need for very complex seismic isolation system as on Earth. The spacecraft needs however to shield the test masses from unwanted forces such as the solar wind or unbalanced gravitational acceleration due to the rest of the spacecraft. To reach the isolation requirements, each proof mass will float inside its housing without any mechanical contact [30]. A combination of electrostatic sensors and capacitive actuators will permit to control all six degrees of freedom of the test masses in order to keep them in their working position and orientation.

The operating frequency range of LISA will be between 0.1 mHz and 1 Hz, inaccessible from ground, with a peak sensitivity of $4 \cdot 10^{-21}/\sqrt{\text{Hz}}$ at around 3 mHz [13]. With these characteristics, LISA will be able to detect G.W. from larger objects, such as the

inspirals and fusions of supermassive binary black holes or compact objects falling into supermassive black holes which emit G.W. in the sub-Hz frequency domain [30].

2.2 Vibration isolation

At most locations on Earth, the motion of the ground roughly separates into three categories, with their corresponding frequency bands [31]. They are

- ≥ 1 Hz : Human activity or high gusting winds which push obstructing bodies as buildings or trees.
- $[0.1, 1]$ Hz : microseismic activity originating from complex interactions of water waves in the oceans and other large bodies of water.
- ≤ 0.1 Hz : Earthquakes and tidal strain caused by the Earth-Moon-Sun system.

As it has been seen in Sec. 2.1, seismic activity is the main source of noise limiting detectors at low frequency, hence it is essential to develop high performance isolation systems to reduce its effects. In this section, the possible methods to do so are reviewed.

2.2.1 Location

Since human activity is the main source of seismic noise above 1 Hz, the first thing to do is to choose a location that will experience the least amount of such noise to build the detector. This place should therefore be away from densely populated areas, railways and frequently used roads. In addition, seismic waves produced by anthropological activity originate at the Earth's surface and propagate mainly along the surface while decreasing in amplitude and depth. Therefore, underground sites are most likely to experience the least amount of such noise in this frequency band [12]. Unfortunately, this only applies to high frequency noise and, in any case, a location is never completely quiet. Consequently, additional isolation techniques are needed to meet the challenging sensitivity requirement of a gravitational wave detector. They fall into two categories, passive and active isolation.

2.2.2 Passive isolation

A representation of a 1 degree of freedom passive isolation system is displayed in Fig. 14. It is essentially composed of three elements: a spring of stiffness k, a damper of damping coefficient c, and the payload of mass m that needs to be isolated.
w denotes the ground motion which is transmitted to the payload through the spring's stiffness. The resulting displacement of the mass from its reference point is noted x.
The system works as a harmonic oscillator whose equation of motion is given by

$$m\ddot{x} + c(\dot{x} - \dot{w}) + k(x - w) = 0. \tag{2}$$

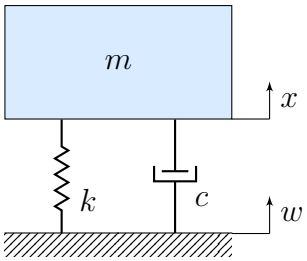

Figure 14: Illustration of 1 dof passive isolation system. The ground motion w is transmitted to the payload's motion x by the spring's stiffness k. The energy loss is represented by the damping coefficient of the damper c.

In the Laplace domain, it becomes

$$ms^2X + cs(X - W) + k(X - W) = 0 \tag{3}$$

where s is the Laplace variable. The transfer function from the ground motion to the payload's is an important quantity called the transmissibility T,

$$T = \frac{X}{W} = \frac{cs + k}{ms^2 + cs + k}. \tag{4}$$

It is a measure of the transmission of ground motion to the payload. The isolation performance of the system depends on the parameters k, c and, m. The transmissibility T for different values of these parameters is shown in Fig. 15 for comparison.

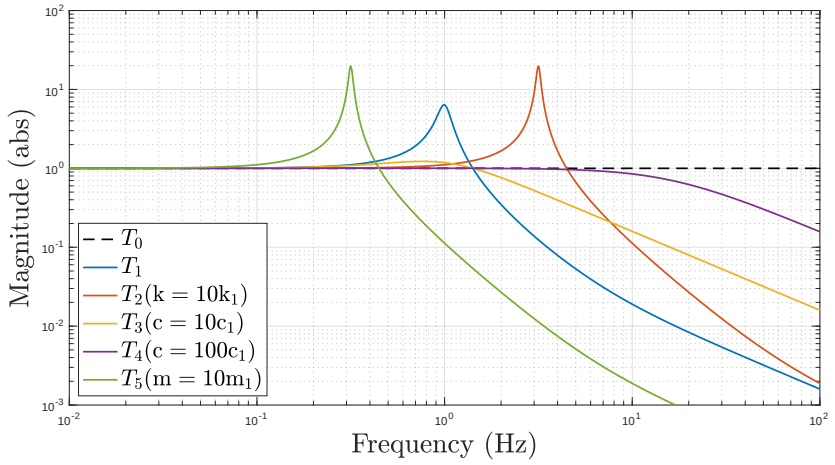

Figure 15: Comparison of the transmissibility of passive isolation systems with different values for parameters k, c, and m. For $T_0 : k_0 = \infty$ N/m. For $T_1 : k_1 = 4\pi^2$ N/m, $c_1 = 1$ N/m/s, $m_1 = 1$ kg. For the other systems, only one parameter is changed from T_1 and is labelled in the figure.

The first system is rigidly mounted on the ground. It is as if it has an infinite rigidity i.e. $k = \infty$ N/m. In this case, $\|T\| = 1$ meaning that the ground motion is fully transmitted to the payload at all frequencies.

The basic isolation system, T_1, has the following parameter values: $k = 4\pi^2$ N/m, $c = 1$ N/m/s and $m = 1$ kg such that its resonance frequency is $f_0 = \sqrt{k/m} = 1$ Hz. Below this frequency, the transfer function tends to the frequency-independent term of Eq. (4). This constant is called the static gain. In this case, its value is 1 which means that the ground motion is fully transmitted to the payload as for the rigid mounted body. At the resonance frequency, the denominator of Eq. (4) cancels out. This implies an amplification of the system's transfer function and $\|T\| > 1$. This means that the payload's motion amplifies that of the ground. In a undamped system, the amplitude increases to infinity. Though, in practice, the amplification is limited as some energy is dissipated by damping. At higher frequencies, the transfer function is dominated by the higher order term, that is $1/(ms^2)$. It is responsible for a -2 slope in logarithmic scale meaning that the system is less and less affected by ground motion as the excitation frequency increases. It is generally called the roll-off. At higher frequency than its resonance, the system is said to be isolated.

To assess the effects of each parameter, the transmissibility of four other systems where only one parameter has been changed in relation to the initial one are also plotted.
The stiffness of the first one (T_2) has been multiplied by a factor of 10. Since it is linked to the resonance frequency, the latter increases and hence the isolation bandwidth is reduced. Moreover, it also has an increasing effect on the critical damping of the system, given by $c_c = \sqrt{km}$. As a result, the damping ratio, $\zeta = c/c_c$, decreases and the amplification of the motion around the resonance frequency is increased. This is why a good isolation system usually requires a low stiffness.

The second system (T_3) has a damping coefficient five times greater than the basic system. It keeps the same resonance frequency while the amplification at resonance is decreased. It comes however at the cost of an augmented transmissibility at higher frequencies, meaning a poorer isolation. Moreover, if the damping is increased well above the critical damping value, the isolation bandwidth can be greatly reduced as it is the case for T_4.

The mass of the last systems (T_5) is ten times that of the initial one. It increases the critical damping the same way as the stiffness does. This results in the same amplification around the resonance. Nevertheless, it lowers the value of the resonance frequency and hence, expands the isolation bandwidth. Though, improvement by adding mass can be difficult in practice because the reduction of the system's resonance frequency by a factor n implies a mass multiplication by a factor n^2. This is especially true for heavy platforms.

Passive isolation stages are appealing as they are relatively inexpensive compared to active stages and they are very good at damping high frequencies vibrations. However, problems

arise for isolating the payload from sub-Hz frequency vibrations since it is difficult to decrease their resonance frequency below a few hertz [32].

2.2.3 Active isolation

When the required vibration isolation cannot be achieved by passive methods, active techniques are used. In this scenario, actuators are used to apply a force on the payload to cancel its motion. Fig. 16 presents a schematic of the single dof system of Fig. 14 augmented with a controller H and actuator f.

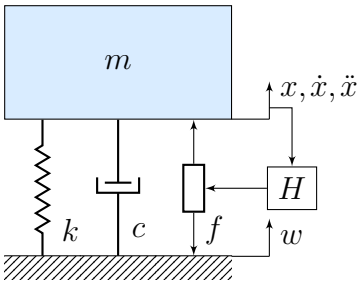

Figure 16: Illustration of 1 dof active isolation system. The ground motion w is transmitted to the payload's motion x by the spring's stiffness k. The energy loss is represented by the damping coefficient of the damper c. A sensor measures the mass' displacement x, velocity $\dot{x}$, or acceleration $\ddot{x}$ and this value is multiplied by the controller H to inject a signal to the actuator.

A sensor is properly placed to measure one state of the mass m. For instance, its displacement $x(t)$ can be measured using a displacement sensor. The controller processes this signal and informs the actuator to inject a force corresponding to the signal x multiplied by the controller.

$$f = -Hx \tag{5}$$

The displacement is not the only variable that can be measured and used in feedback. Velocity and acceleration sensors also exist which measure the payload's velocity $\dot{x}(t)$ and acceleration $\ddot{x}(t)$ respectively.
Similarly to the passive stage, the equation of motion of the system can be derived. In the Laplace domain, it gives

$$ms^2X + cs(X - W) + k(X - W) = f. \tag{6}$$

The transmissibility is thus given by

$$T = \frac{X}{W} = \frac{cs + k}{ms^2 + cs + k + f}. \tag{7}$$

Depending on the type of sensor used, it takes one of the following form

Displacement sensor : $$T_{\text{disp}} = \frac{cs+k}{ms^2+cs+k+H} \tag{8}$$

Velocity sensor : $$T_{\text{vel}} = \frac{cs+k}{ms^2+(c+H)s+k} \tag{9}$$

Force sensor : $$T_{\text{force}} = \frac{cs+k}{(m+H)s^2+cs+k} \tag{10}$$

To compare the performances of each controller, their transmissibility are plotted in Fig. 17 with a constant gain value H. Increasing this value increases the control effort and thus the effects of the controller on the system.

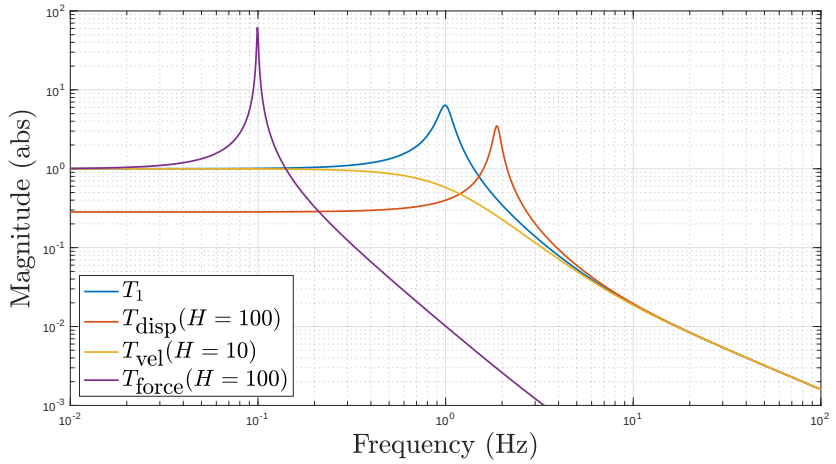

Figure 17: Comparison of the transmissibility of active isolation systems with different types of sensors used for feedback. The value of the control gain is indicated in parenthesis.

The displacement feedback increases the system's resonance frequency while damping a little bit the amplification at resonance. The isolation performances are unchanged at higher frequency but it implements isolation performances below its resonance frequency ($\|T_{disp}\| < 1$). Displacement feedback may also be called a sky-hook spring because the actuator acts as a spring linking the mass to an imaginary point fixed in the sky [33].
The velocity feedback damps the excitation at resonance and keeps the same isolation performances away from it. It may also be called sky-hook damper because actuator acts as a damper linking the mass to an imaginary point fixed in the sky [33]. The acceleration feedback increases the isolation bandwidth by reducing the value of the resonance frequency. However, the effects of the latter are increased and it does not perform any isolation at lower frequency.

Both displacement and acceleration feedback improve the isolation performances of the platform at low frequency. Though, larger control bandwidth can be achieved with displacement feedback especially at very low frequencies. Hence, it is the best candidate for

active seismic vibration isolation.

The resolution of the sensors are not infinite. The sensors can perform accurate measurements down to a certain precision. This value is known as the sensor's resolution. Below it, the sensor's signal is dominated by its noise that is injected in the control loop. Fig. 18 illustrates the active isolation system of Fig. 16 with displacement feedback and the addition of sensor noise n_s.

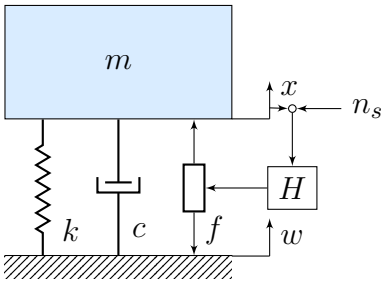

Figure 18: Illustration of a single dof active isolation system with displacement feedback and sensor noise n_s.

The force applied by the actuator on the payload becomes

$$f = -H(x + n_x). \tag{11}$$

The equation of motion in the Laplace domain is then given by

$$ms^2X + cs(X - W) + k(X - W) = -H(X + N_x) \tag{12}$$

which can be written in the following form

$$X = \frac{cs + k}{ms^2 + cs + k + H}W - \frac{H}{ms^2 + cs + k + H}N_x. \tag{13}$$

The maximum performance of the isolation system can be estimated by taking an infinitely large gain H. In this case,

$$\lim_{n_s \to \infty} X = -N_x \tag{14}$$

meaning that the mass motion is dominated by the sensor noise. Therefore, to achieve high level of isolation, the sensor noise must be reduced as much as possible.

3 Theory of control

Control theory is a branch of Applied Mathematics dealing with the use of feedback to influence the behaviour of a system in order to achieve a desired goal.
In this section, the basics of this theory will be laid out with the concept of state space representation, transfer function, and feedback control. A type of optimal controller known as the LQR is then presented. In order to control any physical system, a sufficient knowledge of the state of that system is required. It is achieved through the use of appropriately positioned sensors. Though, in some cases, the sensors are limited by poor sensitivity or just cannot be placed at the required location. Under these circumstances, a method to estimate the unknown states and to develop a control law based on these estimations is necessary. This is the role of the state observer and the Kalman filter that are discussed afterwards.

3.1 State space representation

This section focuses on linear time-invariant (LTI) systems. These are systems that can be described by a series of linear ordinary differential equations and whose response is the same independently of the time. Considering an nth-order system :

$$x^n = a_1 x^{n-1} + a_2 x^{n-2} + ... + a_{n-1}\dot{x} + a_n x \tag{15}$$

where $x^n = \frac{d^n x(t)}{d^n t}$. The following parameters can be defined

$$\begin{aligned} x_1 &= x, \\ x_2 &= \dot{x}, \\ &... \\ x_n &= x^{n-1}. \end{aligned}$$

Eq. (15) may then be expressed as a series of n first order ordinary differential equations as

$$\begin{aligned} \dot{x}_1 &= x_2, \\ \dot{x}_2 &= x_3, \\ &... \\ \dot{x}_{n-1} &= x_n, \\ \dot{x}_n &= a_n x_1 + a_{n-1} x_2 + ... + a_2 x_{n-1} + a_1 x_n \end{aligned}$$

where $(x, \dot{x}, ..., x^{n-1})$ are the n state variables. In matrix form, it can be written as

$$\dot{\mathbf{x}} = A\mathbf{x} \tag{16}$$

where A, a $n \times n$ matrix named the state matrix, characterizes the dynamics of the states and $\mathbf{x}$, named the state vector, is a vector containing the state variables of the system. The system can be extended to take into account the impacts of external inputs. Considering an input vector $\mathbf{u}$ of size p, the system becomes

$$\dot{\mathbf{x}} = A\mathbf{x} + B\mathbf{u} \tag{17}$$

with the $n \times p$ input matrix B. The measurements of the system assessed by sensors are included in an output vector $\mathbf{y}$ of size m. They are a combination of the state variables and the inputs such that

$$\mathbf{y} = C\mathbf{x} + D\mathbf{u} \tag{18}$$

with C the $m \times n$ sensing matrix and D the $m \times p$ feedthrough matrix. The mathematical formalism described by Eq. (17) and (18) is known as a state space representation of the system [34]. It allows to derive the system's outputs and to project its states forward from the knowledge of the system's states and inputs at any given time. A schematic illustration in the form of a block diagram describing the relationship between each vector and matrix is given in Fig. 19.

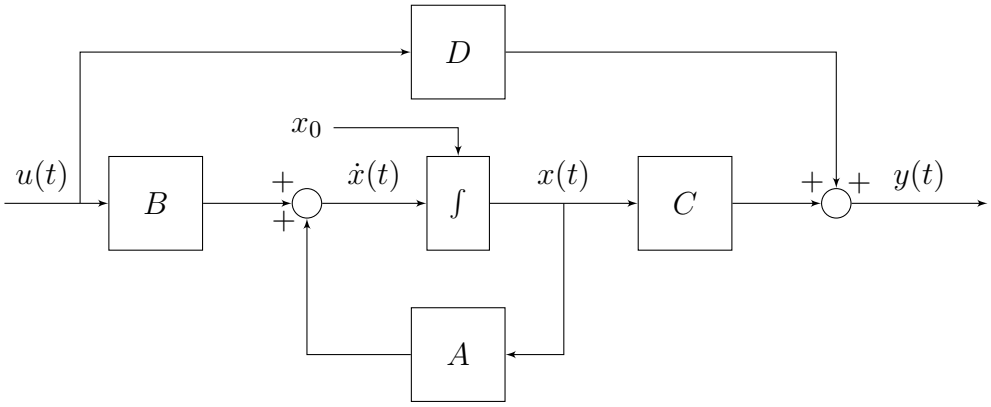

Figure 19: State equation block diagram.

3.2 Transfer function

Solving differential equations in time-domain can be complicated. A useful technique is to transform the differential equation in the time-domain to an algebraic equation in the frequency-domain. This is done by the use of the Laplace transform

$$\mathcal{L}(f(t)) = F(s) = \int_0^\infty f(t)e^{-st}dt \tag{19}$$

where $s = \sigma + i\omega$ is a complex number frequency parameter called the Laplace variable. After applying it to Eq. 17 and 18, they become

$$s\mathbf{X}(s) = A\mathbf{X}(s) + B\mathbf{U}(s), \tag{20}$$

$$\mathbf{Y}(s) = C\mathbf{X}(s) + D\mathbf{U}(s) \tag{21}$$

where the vectors $\mathbf{X}(s)$, $\mathbf{U}(s)$, $\mathbf{Y}(s)$ are respectively the Laplace transforms of the state, input, and output vectors. Eq. (20) and (21) can be combined to get the following relationship

$$\mathbf{Y}(s) = (C(s\mathbb{I} - A)^{-1}B + D)\mathbf{U}(s) \tag{22}$$

$$= H(s)\mathbf{U}(s) \tag{23}$$

where $\mathbb{I}$ is the identity matrix and $H(s)$ is the transfer function matrix with dimensions $m \times p$. It describes the dynamic relation between each input and each output. They are useful tools to study the system's behaviour and design controllers.

3.3 Observability and controllability

The observability and controllability of a system are two important concepts in control design. The former describes a system whose every state $\mathbf{x}(t)$ can be determined from its outputs $\mathbf{y}(t)$ over a finite time interval. It is especially useful when dealing with systems for which some states are not directly measurable. Indeed, in this case, the unmeasurable states must be estimated from the observations in order to construct the feedback control signal. This will be later discussed in Sec. 3.5 with the notion of the observer. Controllability relates to a system whose every state can be brought from any initial value $\mathbf{x}(t = 0)$ to any other, through the action of an input signal $\mathbf{u}$, in a finite amount of time [35].

In control design, the conditions of observability and controllability guarantee the existence of a complete solution to a problem. These two conditions can be translated in algebraic form. The observability matrix ($\mathcal{O}$) and the controllabity matrix ($\mathcal{C}$) of the nth-order system described by Eq. (17) and (18) are defined by

$$\mathcal{O} = \begin{bmatrix} C & CA & CA^2 & \cdots & CA^{n-1} \end{bmatrix}^T, \tag{24}$$

$$\mathcal{C} = \begin{bmatrix} B & BA & BA^2 & \cdots & BA^{n-1} \end{bmatrix}. \tag{25}$$

A sufficient and necessary condition for the system to be observable is that the rank of the observability matrix is equal to the order, or likewise the number of states, of the system i.e. $\text{rank}(\mathcal{O}) = n$. And equivalently, the system is controllable if $\text{rank}(\mathcal{C}) = n$ [34]. Moreover, there is a connection between observability and controllability known as duality.

The dual state equation of the system described by Eq. (17) and (18) is given by

$$\dot{\mathbf{z}} = A^T\mathbf{z} + C^T\mathbf{v}, \tag{26}$$

$$\mathbf{w} = B^T\mathbf{z} + D^T\mathbf{v}. \tag{27}$$

The original realisation (A, B, C, D) is controllable if and only if the dual realisation (A^T, B^T, C^T, D^T) is observable and vice versa [35].

Transfer functions have multiple realisation because, starting with a particular realisation, any valid coordinate transformation yields another state-space realisation with the same dimension. Moreover, they may have realisations of different dimensions. The realisation of a system is said to be minimal if this realisation is of least dimension out of all possible realisations. This concept is linked to observability and controllability in that the realisation of a transfer function is minimal if and only if it is both controllable and observable [35].

Other features of systems in control design, although less powerful, are the stabilizability and detectability. They apply to systems that are not fully observable or controllable. A system is said to be stabilizable if all the uncontrollable eigenvalues of the system are stable i.e. they have a negative real part. In algebraic form it is expressed as

$$\text{if } \operatorname{rank}(A - \lambda\mathbb{I}, B) < n, \qquad \text{then } \operatorname{Re}(\lambda) < 0. \tag{28}$$

It implies that an unstable system can be stabilised by acting on the controllable part of the system [34], [36]. On the other hand, a system is said to be detectable if all the unobservable eigenvalues of the system are stable. It guarantees the existence of an asymptotically stable linear dynamic state observer. The concept of detectability and stabilizability are also dual as observability and controllability [34], [37].

3.4 Feedback control and LQR

As mentioned earlier, the reason for developing control algorithms is to bring a system to a desired position. This task needs to be accomplished while minimizing any delay, overshoot or steady-state errors and ensuring system stability. The controller also aims to a certain degree of optimality. In order to achieve these goals, the controller monitors the system's variables through sensors and compare them with their desired set point values. The difference between them, namely the error, is then used to construct a control vector to be fed back to the system in order to bring the values of these variables to those of the set points. Since the feedback vector is constructed from the system's measurement, the dynamic of the system extended with this type of controller is dependent of its outputs. In

this case, the system is said to be in closed-loop. Otherwise, if its dynamic is independent of its outputs, it is said to be in open-loop [34]. A block diagram exhibiting the interaction of the feedback control law with the system is shown in Fig. 20.

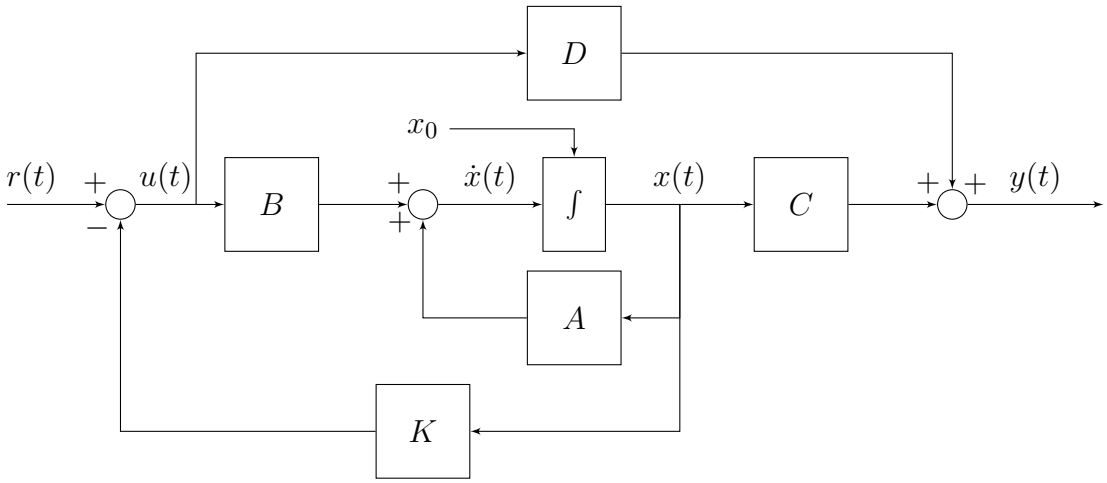

Figure 20: Closed-loop system block diagram.

There are many types of controller but only the well known linear quadratic regulator (LQR) will be discussed through this work. It is of paramount importance as the latter provides an optimal feedback control of the system. This optimal controller is obtained via the minimisation of a quadratic cost function proportional to the measure of the system's response. The parameters of this cost function must be set by the engineer and are chosen in order to reduce the deviations of the system's states from their desired values. For a coninuous-time system described by Eq. (17) and (18), the cost function is given by

$$J_{\mathrm{LQR}} = \int_0^\infty (\mathbf{x}^T Q_{\mathrm{LQR}} \mathbf{x} + \mathbf{u}^T R_{\mathrm{LQR}} \mathbf{u}) dt. \tag{29}$$

The parameters that need to be defined are the entries of the two weighting matrices Q_{LQR} and R_{LQR}. They are positive-definite matrices used to respectively weight the system's states and control power. They are chosen based on specific control criteria and usually require a trial and error process to achieve the desired controller performances. A solution to the optimisation problem of minimising J_{LQR} can be shown to be of the following form

$$\mathbf{u} = -K\mathbf{x} \tag{30}$$

where K defined as $K = R_{\mathrm{LQR}}^{-1} B^T P$ is known as the LQR gain matrix. Matrix P is, for its part, computed by solving the continous-time Riccati differential equation

$$A^T P + PA - PBR_{\mathrm{LQR}}^{-1} B^T P + Q_{\mathrm{LQR}} = 0. \tag{31}$$

The proportional feedback law found in Eq. (30) can then be used to close the system's loop in an optimal way [34]. One of the main constraints of this technique is that this

solution requires complete knowledge of all the system's states which is usually not the case in real-world applications. To overcome this issue, it will be seen that the design of a state observer can be combined with the linear quadratic regulator to efficiently control a system. This type of control is known as a linear quadratic Gaussian (LQG) control.

3.5 State observer and Kalman filter

In this section, the concept of state observer is explained and the Kalman filtering methods for states estimation is discussed.

3.5.1 State observer

When one or more states of a system cannot be directly measured by any sensors, it is of great importance to be able to estimate them in order to develop a feedback control law. A state observer is a dynamic system used for this purpose. The observability condition of the system plays an important role here because a state observer can only be designed if the condition is met. In the event that the observer estimates all of the system's states, it is called a full-state observer [34]. The observer of a continuous-time system described by Eq. (17) and (18) is modeled as

$$\dot{\hat{\mathbf{x}}} = A\hat{\mathbf{x}} + B\mathbf{u} + L(\mathbf{y} - \hat{\mathbf{y}}), \tag{32}$$

$$\hat{\mathbf{y}} = C\hat{\mathbf{x}} + D\mathbf{u} \tag{33}$$

with $\hat{\mathbf{x}}$ and $\hat{\mathbf{y}}$ the vectors of estimated states and outputs respectively. L is the $n \times m$ observer gain matrix. The mathematical model of the observer is basically the same as that of the initial plant where the state and output vectors have been replaced by their estimates and the addition of a term containing the error between the actual measured output $\mathbf{y}$ and its estimate $\hat{\mathbf{y}}$. A block diagram representing the system and state observer is displayed in Fig. 21. The observer inputs are the system's outputs $y(t)$ from sensors and its inputs $u(t)$. The observer exploits these data and produces a state estimate $\hat{x}$ as output.

The error term of Eq. (32) is intended to bring the state estimate $\hat{\mathbf{x}}$ to its actual value $\mathbf{x}$ over time. The condition for convergence is developed hereafter. The estimation error e is defined as the difference between the measured and estimated states,

$$e = \mathbf{x} - \hat{\mathbf{x}}. \tag{34}$$

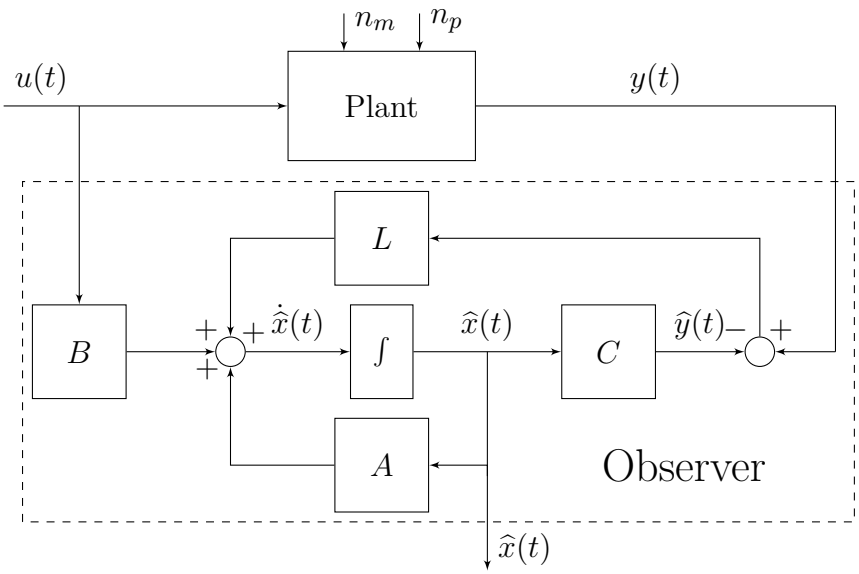

Figure 21: Detailed observer block diagram

The differential equation governing the error signal (the error dynamics) may be derived

$$\begin{aligned}\dot{e} &= \dot{\mathbf{x}} - \dot{\hat{\mathbf{x}}} = A\mathbf{x} + B\mathbf{u} - [A\hat{\mathbf{x}} + B\mathbf{u} + L(\mathbf{y} - \hat{\mathbf{y}})] \\ &= Ae - L\Big([C\mathbf{x} + D\mathbf{u}] - [C\hat{\mathbf{x}} + D\mathbf{u}]\Big) \\ &= (A - LC)e \end{aligned} \tag{35}$$

for which the initial state is given by $e(0) = \mathbf{x}(0) - \hat{\mathbf{x}}(0)$. Since the error dynamics specify a homogeneous linear state equation, this result implies that if the observer could be initialised with no initial error i.e. $\hat{\mathbf{x}}(0) = \mathbf{x}(0) \longrightarrow e = 0$, then $\dot{e}(t) = 0 \ \forall t \geq 0$ and perfect estimation could be achieved at all time. However, since the initial state is presumably unknown, this cannot be accomplished. Instead, the conception of an asymptotically convergent estimate with any initial error can be carried out. For the estimate to be asymptotically convergent, the estimation error has to decay to zero over time. This only occurs if the error dynamics are asymptotically stable which translates into the condition that the eigenvalues of matrix $(A - LC)$ must strictly be in the left-half part of the complex plane. The fulfillment of this requirement depends on the observer gain matrix L which can be chosen accordingly [35]. If the system (A, C) is completely observable, then L can be chosen to place the eigenvalues of $A - LC$ at arbitrary locations in the plane, under the restriction that complex eigenvalues must appear in complex conjugate pairs. As long as (A, C) is at least detectable, then $A - LC$ can be made asymptotically stable by choice of L.

3.5.2 Kalman filter

Various state estimation techniques exist to construct an appropriate observer gain matrix L for the system of concern. One of them is the Kalman filter, also known as linear quadratic estimator (LQE). The kalman filter is an algorithm that computes the observer gain matrix taking into account the different sources of noise present within the system. For example, the measurement noise which represents the noise characteristics of the sensors and the process noise which represents the error on the model dynamics and the input response. It is of great importance because developing an observer without considering them might make the state estimation very sensitive to uncorrelated noises. The accuracy of the estimation would consequently be decreased. Taking into account the measurement and process noise, $\mathbf{n}_m$ and $\mathbf{n}_p$ respectively, Eq. (17) and (18) describing a linear continuous-time system become

$$\dot{\mathbf{x}} = \mathbf{A}\mathbf{x} + \mathbf{B}\mathbf{u} + \mathbf{B}_n\mathbf{n}_p, \tag{36}$$

$$\mathbf{y} = \mathbf{C}\mathbf{x} + \mathbf{D}\mathbf{u} + \mathbf{n}_m. \tag{37}$$

For classical Kalman filter design, it is assumed that the noises are zero-mean normal Gaussian stochastic processes with known statistical properties such that

$$E[\mathbf{n}_m] = E[\mathbf{n}_m] = 0, \tag{38}$$

$$E[\mathbf{n}_p\mathbf{n}_p^T] = Q_n, \tag{39}$$

$$E[\mathbf{n}_m\mathbf{n}_m^T] = R_n, \tag{40}$$

$$E[\mathbf{n}_p\mathbf{n}_m^T] = N_n \tag{41}$$

where E denotes the expectation operator. Q_n, R_n and N_n are the noise covariance matrices respectively linked to the process noise, the measurement noise and finally the correlation between the two. If the two noise sources are not correlated, N_n is simply null [38]. Given the statistical properties of the various noise sources and knowledge of the internal dynamics of the system, the Kalman filter computes an optimal Kalman gain matrix L by minimising the mean square of the estimation error given by

$$J = e^T e = (\mathbf{x} - \widehat{\mathbf{x}})^T(\mathbf{x} - \widehat{\mathbf{x}}) \tag{42}$$

$$= \mathrm{tr}(P) \tag{43}$$

where P is the estimation error covariance matrix defined by $P = E[(\mathbf{x} - \widehat{\mathbf{x}})(\mathbf{x} - \widehat{\mathbf{x}})^T]$. It can be shown that for the new system characterised by Eq. (36) and (37), the general solution of the observer gain matrix in Eq. (32) is given by

$$L = (PC^T + B_nN_n)R_n^{-1}. \tag{44}$$

Matrix P assures the minimisation of J and is computed by solving the following Riccati differential equation

$$\begin{aligned}\dot{P} =&[A - B_n N_n R_n^{-1} C]P + P[A - C R_n^{-1} N_n B_n]^T \\ &- P C^T R_n^{-1} C P + B_n[Q_n - N_n R_n^{-1} N_n^T] B_n^T\end{aligned} \tag{45}$$

When implementing a Kalman filter in practice, the noise covariance matrices must be assessed. The measurement noise covariance can usually be inferred from experimental measurements. Small values for R_n implies that strong confidence is attributed to the sensors measurements or, in other words, that the sensors are very reliable. With regard to process noise, it is less straight forward. This noise source represent the uncertainty of the mathematical model governing the plant. High values of Q_n means a lower reliance on the model in the case of a poorly defined one. The noise covariance matrices can be tuned in order to find the right balance between the filter's reliance on sensor measurement and on the plant's model. The choice to be made depends on the system of interest [39].

Other types of filters not limited to linear systems with Gaussian distributed noises exist. For instance, Extended (EKF) or Unscented (UKF) Kalman filter may be used when dealing with non linear systems. Moreover, the particle filter is another type of filter that is able to approximate any type of noise distribution. Though, it comes at the expense of high computational cost [40].

3.6 LQG control

The linear–quadratic–Gaussian (LQG) control is one of the most fundamental optimal control and concerns linear systems driven by additive white Gaussian noise. As mentioned earlier, it simply combines a Kalman state observer with a linear quadratic regulator (LQR) into an LQG regulator to be used as feedback in a closed-loop system. An important feature is that the LQR and the state observer can be designed independently. Indeed, the optimal Kalman state estimate $\widehat{\mathbf{x}}$ is independent of the LQR parameters. Hence, the solution of the LQG problem can be found by simply replacing the estimate computed beforehand in Eq. (30) giving the LQG feedback law

$$\mathbf{u} = -K\widehat{\mathbf{x}}. \tag{46}$$

This is known as the separation principle. The problem can be broken down into two distinct parts making the controller design much easier. A block diagram representing the LQG control on a noisy plant may be seen in Fig. 22. It also features how the reference input r and the integral action can be included in the loop. The control $r - \mathbf{y}$ is integrated and the regulator K is designed for the plant augmented with integrator states [41], [42].

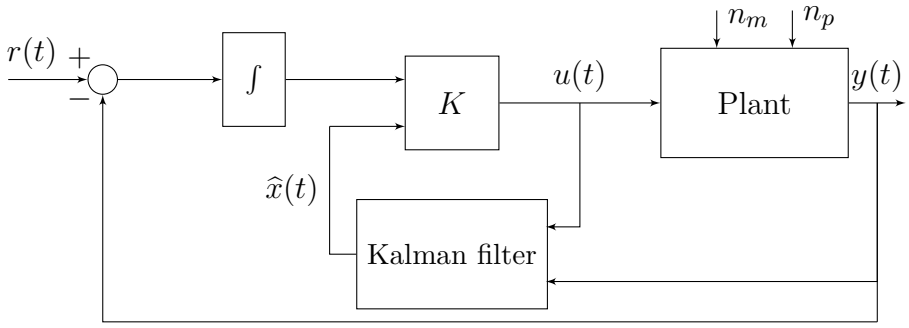

Figure 22: LQG controller block diagram.

4 Experimental platform

The aim of this section is to describe the experimental isolation platform for which the controller will be developed. This hybrid platform composed of an active stage placed on top of a passive stage is shown in Fig. 23. The passive platform is made of a rectangular table set on four springs while the active platform is made of an hexagonal table of 157 kg supported by three Yuanda isolators (see Sec. 4.3). On top of it, three sensor units in charge of giving feedback on the platform's states are placed. They are each composed of one horizontal and one vertical inertial sensor, respectively HINS and VINS, sealed inside a vacuum chamber. The information from the sensors are fed to a digital controller which builds the control law which will be sent to the other devices in the form of a current. The signal is then transmitted to voice coil actuators inside the isolators after being magnified in a current amplifier [32]. The main components of the experimental platform are discussed in the following sections.

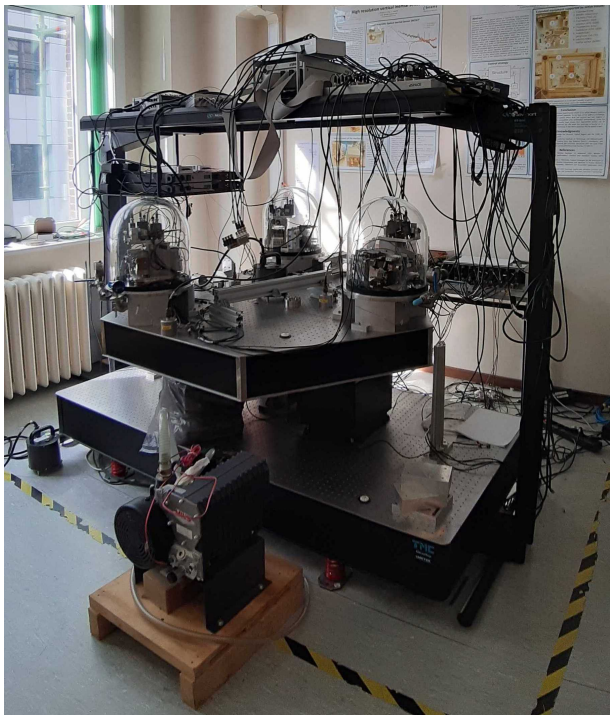

Figure 23: Picture of the experimental platform located at the University of Liège used for the study and development of isolation techniques.

4.1 Inertial Sensors

The sensors discussed in Sec. 2.2.3 were considered as absolute sensors so that they were able to measure the absolute motion of the ground and masses. However, in practice, the sensors measure the relative displacement between two objects. Therefore, in order to perform absolute measurements, sensors measuring the relative motion of the mass with

respect to an inertial reference are used. These are called inertial sensors. Though, they can only provide absolute measurements in a specific frequency range depending on their parameters [43].

The schematic representation of an inertial sensor is presented in Fig. 24. It consists of an inertial mass (m_i) connected to the payload (m) by a suspension system, itself composed of a spring (k) and a damper (c). x and x_i depict the absolute displacement of the payload and the inertial mass respectively. The relative displacement between the two bodies, noted y, is what is actually measured.

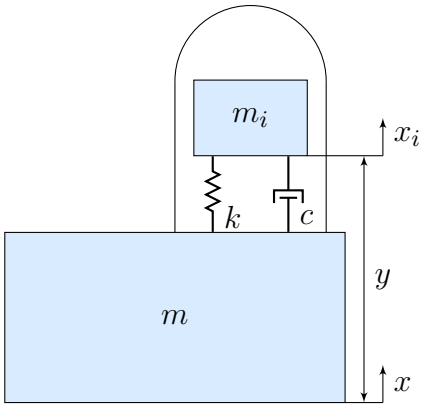

Figure 24: Illustration of an inertial sensor measuring the motion of mass m. The signal measured is the relative displacement y between the payload with absolute displacement x and the inertial mass with absolute displacement x_i.

The dynamic of the system is described by the following equation

$$m_i\ddot{x}_i + c(\dot{x}_i - \dot{x}) + k(x_i - x) = 0. \tag{47}$$

Knowing that $y = x_i - x$, one can write this equation in terms of y. One gets

$$m_i\ddot{y} + c\dot{y} + ky = -m_i\ddot{x} \tag{48}$$

which becomes, in the Laplace domain,

$$m_i s^2 Y(s) + csY(s) + kY(s) = -m_i s^2 X(s). \tag{49}$$

The transmissibility from the absolute displacement of the payload (X) to the relative displacement between the inertial mass and the payload (Y) can be deduced

$$T_{xy}(s) = \frac{Y(s)}{X(s)} = \frac{-m_i s^2}{m_i s^2 + cs + k}. \tag{50}$$

The magnitude of the frequency response of T_{xy} is shown in Fig. 25.
Above the system's resonance frequency ($w_0 = \sqrt{k/m}$) set at 1 Hz, the measurement of

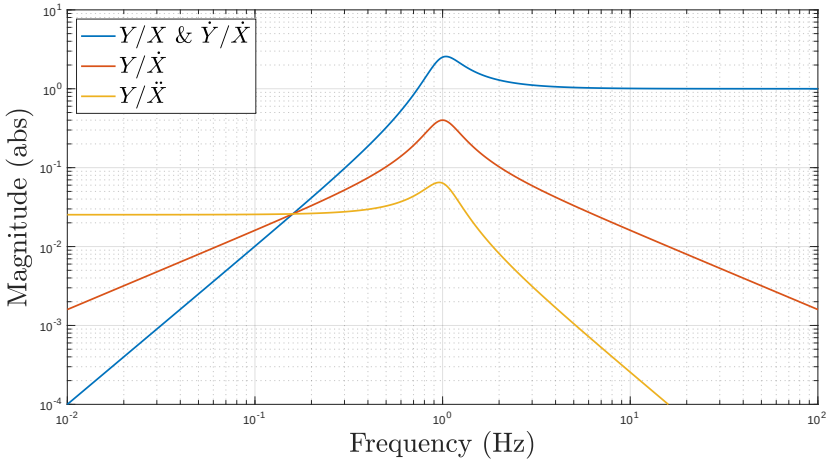

Figure 25: Various transmissibilities of the inertial sensor linked to a payload from Fig. 24.

the relative displacement is a perfect estimator of the payload's absolute displacement. Indeed, it is seen from Eq. 50 that, for high frequency values, the transmissibillity between the two quantities is $\|T_{xy}\| = 1$. It is also the case for the transmissibility between the relative speed between the two masses ($\dot{Y}$) and the absolute speed of mass m ($\dot{X}$) because $T_{\dot{x}\dot{y}}(s) = T_{xy}(s)$.
In addition, the transmissibility from the payload's speed to the relative displacement ($Y/\dot{X}$) and from the payload's acceleration ($\ddot{X}$) to the relative displacement ($Y/\ddot{X}$) are plotted. Their expressions are given by

$$T_{\dot{x}y}(s) = \frac{Y(s)}{\dot{X}(s)} = \frac{-m_i s}{m_i s^2 + cs + k}, \tag{51}$$

$$T_{\ddot{x}y}(s) = \frac{Y(s)}{\ddot{X}(s)} = \frac{-m_i}{m_i s^2 + cs + k}. \tag{52}$$

As for $T_{xy}(s)$, at low frequency, the transmissibility between the payload's acceleration and the relative displacement tends towards a constant, $\|T_{\ddot{x}y}\| = m_i/k$. As it may be seen in Fig. 25, it means that Y is a perfect estimator of $\ddot{X}$ below the system's resonance frequency. Although, this time, the amplitude of the motion transmitted is scaled by $1/w_0^2$. Hence, the accelerometor's sensitivity is improved by decreasing the resonance frequency.

In the experimental set up, displacement inertial sensors are used. They were chosen for their efficiency for seismic vibration isolation as demonstrated in Sec. 2.2.3. To be sensitive in the bandwidth of interest ($[0.1, 10]$ Hz), they have a much lower resonance frequency. Yet, the spring-mass system is responsible of additional sources of limitations for the sensor. For instance, because the spring is soft, its internal modes might also be in the control bandwidth. The characteristics and resolution of these sensors are discussed in details in [33].

4.2 Current amplifier

The measurements from the sensors are fed to the controller which uses them to construct a feedback vector signal. This signal is then transmitted to the actuators which isolate the platform. However, the input signal from the controller is weak and hence, the actuators cannot produce the appropriate force with the input current. To overcome this problem, a current amplifier is inserted between the controller and the actuators. It is an electronic circuit used to increase the magnitude of current of the input signal by a fixed multiple which is then fed to the succeeding device. The current amplifier used in the experiment converts the input voltage into current with a gain of 1/5 A/V [32]. It has been showed that it does not introduce any phase delay between the signal injected in the current amplifier and the output signal in the control bandwidth . Unlike above 100 Hz where the capacitors inside the current amplifier start to have an effect.

4.3 Yuanda isolators

Yuanda isolators are active vibration isolators made by *Yuanda Tech* which feature active control in all 6 degrees of freedom. A picture of the three isolators supporting the hexagonal table is shown in Fig. 26. They contain horizontal and vertical springs and adaptive negative stiffness springs in the vertical direction. The latter are used to reduce the effective stiffness of the isolator in the vertical direction without influencing its static load-supporting capability. It allows to have a low resonance frequency system which is essential for low-frequency vibration isolation [44]. In addition, there are a pair of horizontal and vertical voice coil actuators responsible for exerting the appropriate force on the hexagonal table to cancel its motion.

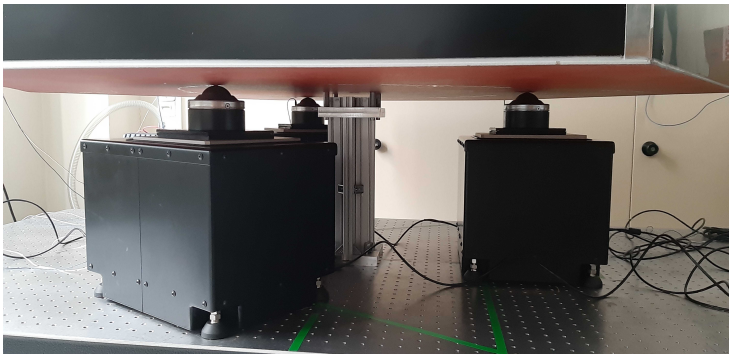

Figure 26: Picture of the three isolators. A sphere is used to have the smallest contact point between the isolators and the hexagonal table. The guide in the center is not in contact with the hexagonal table. It is only placed there for safety reasons in case of an accident.

Fig. 27 shows a schematic of a linear voice coil actuator. They are based on the electromagnetic force exerted on a charged particle moving in a magnetic field, also called the Lorentz force. They are several design types but here is only presented the moving

coil design. A stationary cylindrical permanent magnet produces a radial magnetic field. Housed inside the permanent magnet cylinder is a coil that is wrapped around a non-conducting structure (coil holder). The permanent magnet is housed in a ferromagnetic cylinder that is open at one end and has a "core" through its middle, which is necessary for completing the magnetic circuit. The coil assembly is free to ride in the air gap between this core and the interior surfaces of the permanent magnet.

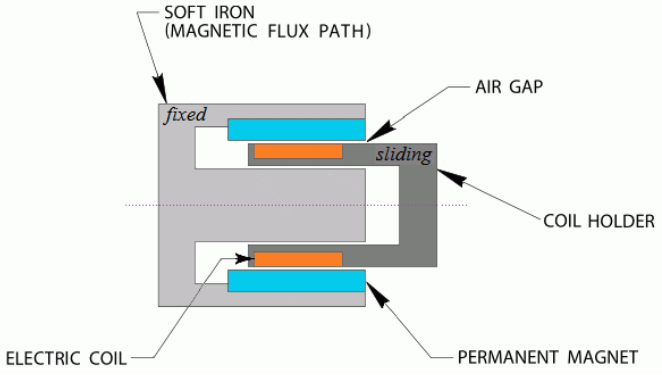

Figure 27: Schematic of a linear voice coil actuator and its components. Retrieved from [45].

When a current is applied to the coil, a force generated by interaction with the permanent magnetic field is exerted on it. The coil holder, linked to the payload in some way , is moved by the force so as to reduce the payload's motion. The magnitude of the applied force is proportional to the current passing through the coil I and is expressed as

$$F = T_a I \tag{53}$$

with T_a the transducer constant of the actuators which depends on the characteristics of the voice coil [45], [46]. The transducer constant is 2.8 N/A for horizontal voice coils and 2 N/A for vertical ones. The isolators are designed to support a weight between 50 kg and 125 kg each and they can be leveled independently to tune the static inclination of the payload [32].

5 Controller development

In order to study the behaviour of the experimental isolation platform and design an appropriate controller for it, a representative model as accurate as possible has been developed with the *Simscape* library from *Matlab* [47]. It is an appropriate tool as it allows to model the interaction between bodies under the gravity field and CAD drawings of each part of the system can easily be imported in the model. In this section, the plant's model will first be described as well as some of its features like its observability and stability. Next, a full-state observer to estimate its unknown states is developed. After that, an LQR controller is designed with *Matlab* and combined with the state observer to produce the LQG regulator. Then, a band-pass filter to limit the controller in the bandwidth of interest is implemented. Finally, a noise budget of the system is performed to show that good signal to noise ratio is achieved. And hence, that the plant can efficiently be controlled in the $[0.1, 10]$ Hz bandwidth with the LQG controller designed.

5.1 Plant model

The model representing the full isolation platform and its dynamic is established in [32]. However, this work is actually based on a simplified version of this model. Indeed, in the model used, the passive stage of the structure has been ignored. The plant representing the system employed to develop the controller is obtained by linearization of the model just mentioned. The plant is composed of 24 states representing the reduced system. Twelve of them describe the dynamics of the hexagonal table moving in six dimensions. Of these twelve, six correspond to translations along the x, y and z directions (one position (x, y, z) and one velocity (v_x, v_y, v_z) for each) and the other six to rotations about the x, y, and z axis (one angle (θ_x, θ_y, θ_z) and one angular velocity (ω_x, ω_y, ω_z) for each). The twelve states remaining describe the dynamics of the six inertial sensors, each moving in two dimensions (one angle (θ_{H1} θ_{H2} θ_{H3} θ_{V1} θ_{V2} θ_{V3}) and one angular velocity (ω_{H1} ω_{H2} ω_{H3} ω_{V1} ω_{V2} ω_{V3}) for each sensor). The measurements taken by the inertial sensors are the plant's outputs. There are three horizontal and three vertical inertial sensors for a total of 6 outputs (HINS1 VINS1 HINS2 VINS2 HINS3 VINS3). Finally, the plant has 6 inputs that come from the three horizontal and three vertical actuators in the isolators placed below the hexagonal table (H1 V1 H2 V2 H3 V3). In state space form, it gives

$$\begin{aligned} \dot{\mathbf{x}} &= A\mathbf{x} + B\mathbf{u} \\ \mathbf{y} &= C\mathbf{x} + D\mathbf{u} \end{aligned} \tag{54}$$

with

$$\mathbf{x} = [\mathbf{x}_{\text{HT}}; \mathbf{x}_{\text{INS}}], \tag{55}$$

$$\mathbf{x}_{HT} = [x\ y\ z\ v_x\ v_y\ v_z\ \theta_x\ \theta_y\ \theta_z\ \omega_x\ \omega_y\ \omega_z]^T, \tag{56}$$

$$\mathbf{x}_{INS} = [\theta_{H1}\ \theta_{H2}\ \theta_{H3}\ \theta_{V1}\ \theta_{V2}\ \theta_{V3}\ \omega_{H1}\ \omega_{H2}\ \omega_{H3}\ \omega_{V1}\ \omega_{V2}\ \omega_{V3}]^T, \tag{57}$$

$$\mathbf{u} = [\text{H1 V1 H2 V2 H3 V3}]^T, \tag{58}$$

$$\mathbf{y} = [\text{HINS1 VINS1 HINS2 VINS2 HINS3 VINS3}]^T. \tag{59}$$

Some important features of the system's plant can be highlighted. First, all of its poles have a negative real part. Hence, the plant is stable. This means that whatever disturbance is acting on the platform, it will stabilise itself without any help from a controller. Hence, the control loop developed hereafter only serves to provide additional isolation performances.

It has been said in Sec. 3.2 that a Laplace transform could be applied to the state space equation, Eq. (54), to yield the relation

$$\mathbf{Y}(s) = H(s)\mathbf{U}(s) \tag{60}$$

where $H(s)$ is the 6×6 transfer function matrix describing the dynamic relation between each input and each output of the plant. These relations give important information as they describe the reaction of the sensors when the actuators are excited. The diagonal elements of $H(s)$ are the relation between each actuator and his corresponding inertial sensor. For example H_{11} is the relation between the first horizontal actuator (H1) and the first horizontal inertial sensor (HINS1) placed right above it on the hexagonal table. They are the most important elements of H as exciting an actuator directly affects its corresponding sensor. Thus, the control law is designed by principally studying these elements. The transfer function from H1 to HINS1 and V1 to VINS1 in the bandwidth $[0.1, 10]$ Hz are shown in Fig. 28. It is seen that the magnitude of both transfer functions is smaller than unity in the whole frequency range. This implies that the initial plant already produce some isolation without active control. Furthermore, its isolation performances is slightly better in the vertical direction than in the horizontal one. The peaks that may be seen in the magnitude graphs of the bode plots correspond to resonances of normal modes of the isolation platform. Those appearing between 0.1 Hz and 0.2 Hz correspond to the resonances of the inertial sensors. The resonances around 1 Hz for the transfer function between horizontal elements and around 2-3 Hz for the transfer function between vertical elements correspond to the isolator's horizontal and vertical suspension modes respectively. These internal modes need to be actively controlled to increase the isolation performances of the platform. The phase graphs of the bode plots, wrapped here

between -180° and 180°, give information about the stability of the system with the gain and phase margin. The gain margin is the distance between the magnitude curve and the 0 db line (1 in absolute unit) at the phase crossover frequency, i.e. where the Bode phase plot equals 180°. It refers to the factor by which the gain must be increased to reach neutral stability i.e. the 0 db line. The phase margin is the distance between the phase curve and the -180° line at the gain crossover frequency, i.e. where the Bode gain plot crosses the 0 dB line. It refers to the amount of phase which can be increased or decreased without making the system unstable.

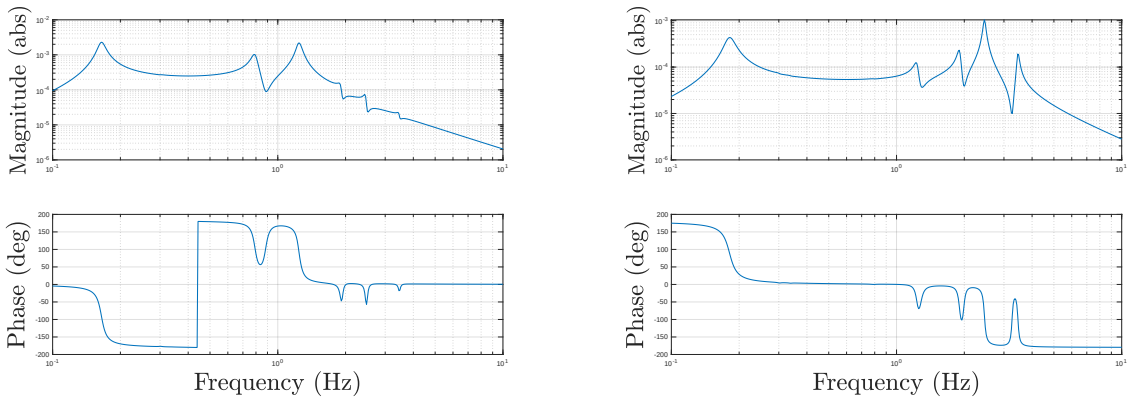

(a) H1 to HINS1 (b) V1 to VINS1

Figure 28: a) Bode plot of the plant's transfer function from actuator H1 to inertial sensor HINS1. b) Bode plot of the plant's transfer function from actuator V1 to inertial sensor VINS1.

Moreover, all the sensors are affected when an actuator is excited. Hence, matrix $H(s)$ contains off-diagonal elements that must also be considered. The six actuators and sensors are said to be coupled. It complicates the design of the controller because the system cannot be broken down in six single-input single-output system (SISO). Instead, it is a multiple-input multiple-output system (MIMO). This is one of the reason why an optimal controller is a good control option as it takes care of these coupling terms which is hard to do when designing a classical control law. The coupling between H1 and VINS1 is illustrated in Fig. 29. Resonances may be seen to occur between 0.8 Hz and 3 Hz. They result from the coupling between the horizontal actuator and the vertical inertial sensor. The dynamic of the vertical sensor is thus also affected by the horizontal suspension modes of the horizontal actuator, although less strongly than the horizontal sensor. Care should thus be given to these coupling terms when designing the controller as increasing the controller gain for the diagonal elements of H may increase and worsen the dynamic of the off-diagonal elements.

As an observer needs to be implemented to estimate the system states, an important

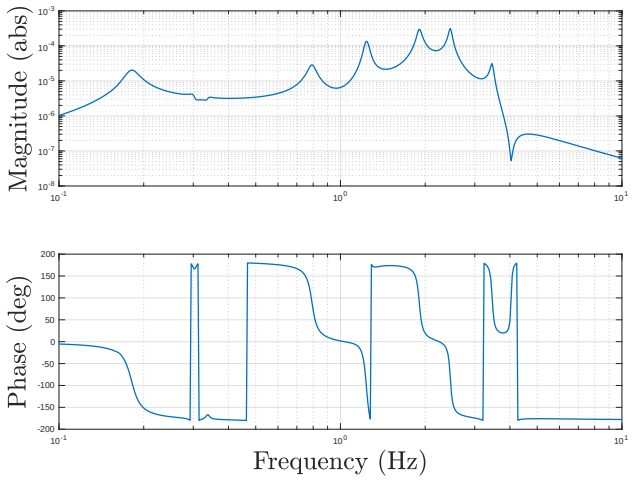

Figure 29: Bode plot of the plant's transfer function from actuator H1 to inertial sensor VINS1

characteristic of the plant is its observability. The system is reassuringly found to be fully observable meaning that all its states can be determined from its outputs. This guarantees the possibility to develop a full-state observer. The plant is also found to be fully controllable so that each of its state can be brought to any value through the action of the input signal. These two conditions guarantee the possibility to design an optimal controller for the system.

5.2 Observer

The twenty-four states of the isolation platform cannot be measured directly. Instead, only the measurements from the inertial sensors are available. Hence, in order to develop a feedback law to control the system in the form of Eq. 30, its states must be estimated by the means of an observer. A full-state observer will therefore be created. As the system is observable, designing an observer is known to be feasible but it must achieve an appropriate accuracy to be able to design a robust controller based on these estimates.

It has been said in Sec. 3.5.2 that the Kalman filter could construct an optimal estimator given the plant state space model and known input and measurement noises. This is what will be used here. The plant is first extended to take noises into account. An input disturbance has been added to each of the six inputs of the system and measurement noise has been added to the measurements. The noise terms are assumed to be Gaussian distributed with zero mean. The state equations describing the platform's dynamic, Eq. (54), become

$$\dot{\mathbf{x}} = A\mathbf{x} + B\mathbf{u} + B_{\mathrm{n}}\mathbf{n_p} \tag{61}$$

$$\mathbf{y} = C\mathbf{x} + D\mathbf{u} + \mathbf{n_m} \tag{62}$$

where $B_{\mathrm{n}} = B$, $\mathbf{n_p} = [\mathrm{H1_d\ V1_d\ H2_d\ V2_d\ H3_d\ V3_d}]^T$ the process noise vector representing the disturbances on each input, and $\mathrm{n_m}$ the measurement noise vector. The noise covariance matrices must now be defined and are functions of the system's noise properties. The measurement noise covariance matrix is usually assessed by experimental tests. Though, here, the matrices have only been guessed and chosen to yield the best possible results as well as an acceptable stability margin. The chosen matrices are the following

$$Q = \mathbb{I}_{6\times 6}, \tag{63}$$

$$R = 10^{-17} \cdot \mathbb{I}_{6\times 6}, \tag{64}$$

$$N = \begin{bmatrix} 0 & \dots & 0 \\ \vdots & & \vdots \\ 0 & \dots & 0 \end{bmatrix}_{6\times 6} . \tag{65}$$

Very low measurement noise have been assumed with respect to process/input noises. In addition, the noise sources are said to be uncorrelated. A steady state Kalman filter is constructed with the *Kalman* function of matlab. The latter computes the observer gain matrix L to be used in the observer state equation, cfr Eq. (32). With this in hand, the state and and output estimates, $\hat{\mathbf{x}}$ and $\hat{\mathbf{y}}$, can be computed.

To asses the performances of the observer, a comparison between the time response of the system's states and their respective estimates to an input disturbance is performed. The input disturbance, represented in Fig. 30, is a sine wave with frequency logarithmically swept from 0.1 Hz and 10 Hz with an amplitude of 1 μm. This has been chosen since this is the range of frequency that are targeted for isolation. Moreover, the relative precision of the observer is the same regardless of the disturbance amplitude. In addition, a white Gaussian noise with zero mean, 0.25 variance and amplitude of 10^{-2} μm has been summed up to the sine wave as real seismic vibrations are not perfect oscillation signals. The sweep of the wave was chosen as logarithmic so that the sinusoidal signal goes from 0.1 Hz to 1 Hz during the first half of the disturbance duration and from 1 Hz to 10 Hz during the remaining time. This way, the sub-Hz perturbations are as well represented as the super-Hz. This input disturbance is introduced on all the six actuator inputs to simulate ground vibration.

The study will only be carried out on a small number of states representative of the

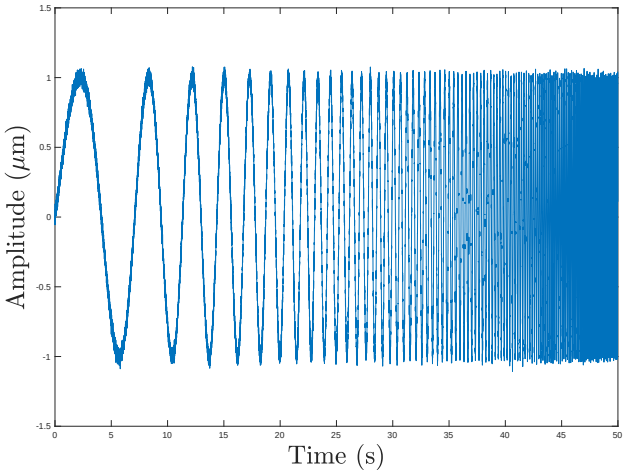

Figure 30: Sine swept input signal from 0.1 Hz to 10 Hz applied to the the six actuators to simulate ground motion. It has zero mean, 0.25 variance and an amplitude of 1 μm.

whole plant as it would be redundant otherwise. For the hexagonal table, four states are considered. They are the position and velocity along the x-direction and the angle and angular velocity around the x-axis. The components related to the other axis yield similar results. Similarly, regarding the inertial sensors, one horizontal and one vertical sensors are studied. Both their angle and angular velocity are considered for a total of four states.

5.2.1 Hexagonal table

The time response of the four states considered for the hexagonal table as well as their estimates to the input disturbance are shown in Fig. 31. They all have a similar responses with higher amplitude reached between 25 s and 50 s corresponding to oscillations with frequencies above 1 Hz. The maximum amplitude reached by the position and angle states are 10^{-4} μm for an input amplitude of 1 μm. This suggests that some passive isolation is already taking place in the platform. Regarding the velocity counter part of these two states, their amplitude amplification between low and high frequency excitation is logically even greater. Indeed, since both the motion amplitude and frequency increase, higher amplitude must be reached at even greater speed, resulting in a large velocity increase.

The observer's state estimates seem to represent the actual system states very well. To assess how well this is actually achieved, graphs representing the error between the states and their estimates may be seen in Fig. 32. They all have an accuracy of 10^{-5} or better compared to the initial input amplitude. Moreover, the error's amplitude tends to decrease as the frequency excitation increases for the states representing the position and velocity of the hexagonal table. They roughly gain an order of magnitude of precision. Though, the estimation error of the states corresponding to the angle and angular velocity

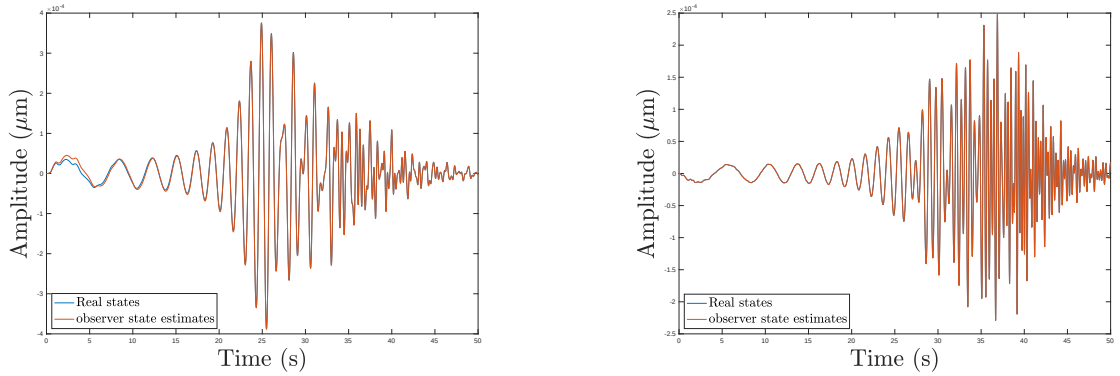

(a) x (b) v_x

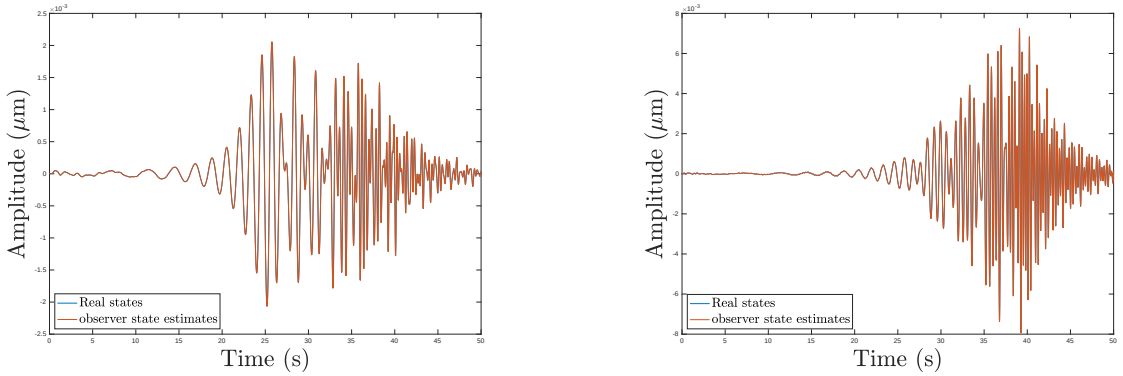

(c) θ_x (d) ω_x

Figure 31: Time response of some of the hexagonal table's states to a sine disturbance logarithmically swept between 0.1 Hz and 10 Hz and with an amplitude of 1 μm.

are already very small for low frequency excitation with an order of 10^{-8} for the former and 10^{-7} for the latter. These values can be put into perspective of the amplitude of motion of the states needed to be estimated. Since the amplitude of motion of the position of the hexagonal table is around 10^{-5} at low frequency and 10^{-4} at high frequency and its estimation is of the order of 10^{-6} at low frequency and 10^{-7} at high frequency, it suggests that the precision of the estimation is roughly 10 % at low frequency and 0.1 % at high frequency. Similarly for the other states, the observer reaches an accuracy of 0.1 % at low frequency and 10^{-3} % at high frequency for the velocity. Considering the angle and angular velocity, an accuracy of 1 % is achieved for low frequency and a factor of one hundred better for high frequency. As a result, it can be concluded that the system's state estimations are less good at low frequency which might lead to more difficulties at isolating the platform in the lowest part of the control bandwidth. However, as the platform resonances occur at frequencies of 1 Hz or more, it is these frequencies that are essential to isolate effectively. Also, the table position is the poorest represented state and will limit the performance of the controller. Though, it will be seen that its

estimation is accurate enough to yield an efficient controller.

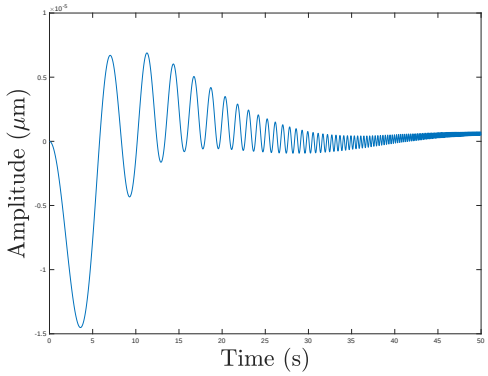

(a) $\Delta x = \widehat{x} - x$

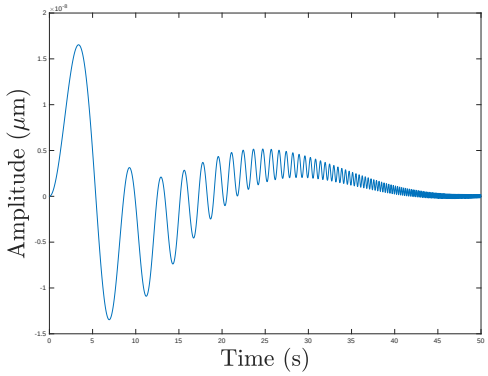

(b) $\Delta v_x = \widehat{v}_x - v_x$

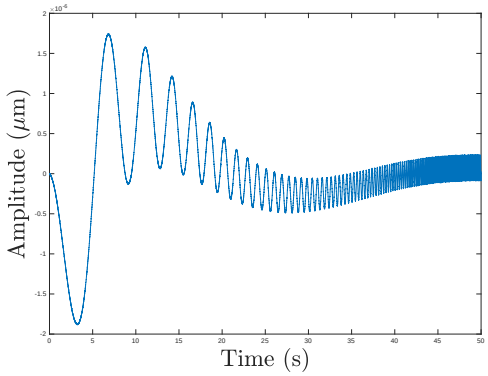

(c) $\Delta \theta_x = \widehat{\theta}_x - \theta_x$

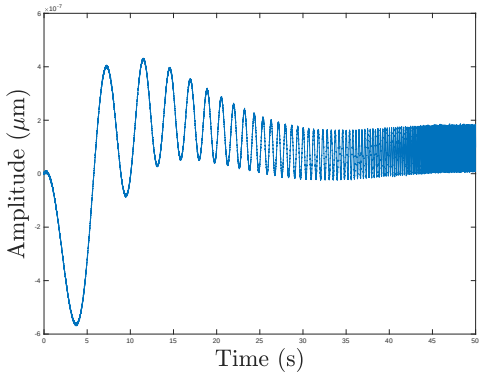

(d) $\Delta \omega_x = \widehat{\omega}_x - \omega_x$

Figure 32: Error between the hexagonal table's state estimates and their actual value for the time response illustrated in Fig. 31.

The error amplitude and the estimation accuracy of all the hexagonal table states are given in Tab. 1. They are roughly separated into a low and high frequency value as it has been seen that resonances and hence high amplitude responses happen in the high frequency part of the control bandwidth i.e. $[1, 10]$ Hz. The error is seen to be of the order of 10^{-5} μm or lower for all the states with the velocity errors usually smaller. As for the accuracy of the state estimations, it is always better for high frequency excitation with a value of at least 0.1 %. For low frequency excitation, the table's position in the x-direction and its angle around the z-axis are the least well represented. Besides them, the state estimation accuracy is of 1 % or better.

	x		y		z		v_x		v_y		v_z	
	LF	HF	LF	HF	LF	HF	LF	HF	LF	HF	LF	HF
Error (m)	1e-6	1e-7	1e-5	1e-6	1e-6	1e-6	1e-8	1e-9	1e-8	1e-8	1e-6	1e-6
Accuracy (%)	10	0.1	1	0.1	0.1	0.1	0.1	1e-3	0.1	1e-2	1	0.1

	θ_x		θ_y		θ_z		ω_x		ω_y		ω_z	
	LF	HF	LF	HF	LF	HF	LF	HF	LF	HF	LF	HF
Error (m)	1e-6	1e-7	1e-6	1e-6	1e-6	1e-6	1e-7	1e-7	1e-7	1e-7	1e-6	1e-6
Accuracy (%)	1	1e-2	1	0.1	10	0.1	1	1e-2	1	1e-2	0.1	1e-2

Table 1: Estimation error and representation accuracy of the hexagonal table's states when subjected to a sine disturbance logarithmically swept between 0.1 Hz and 10 Hz and with an amplitude of 1 μm

5.2.2 Inertial sensor

A similar study is done for the states of the inertial sensors. The time response of the states describing the dynamic of the horizontal and vertical inertial sensors are shown in Fig. 33.

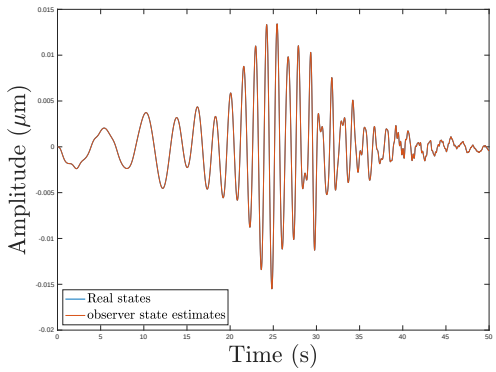

(a) θ_{H1}

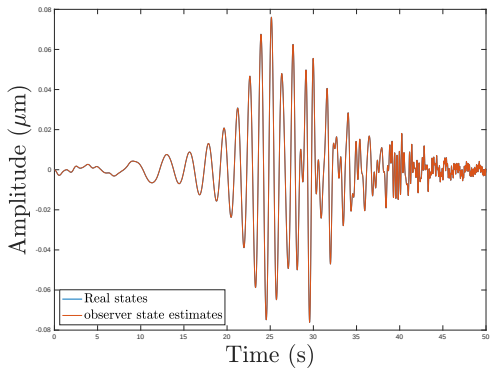

(b) ω_{H1}

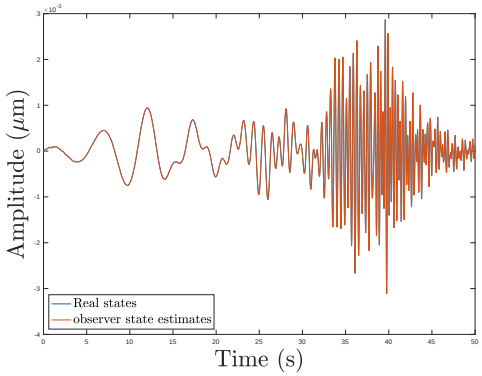

(c) θ_{V1}

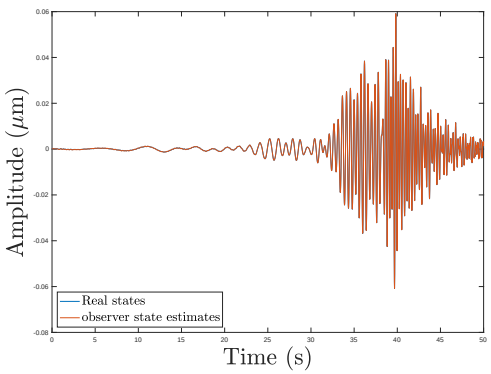

(d) ω_{V1}

Figure 33: Time response of HINS1 and VINS1's states to a sine disturbance logarithmically swept between 0.1 Hz and 10 Hz and with an amplitude of 1 μm.

For the horizontal inertial sensor, the states motion amplitude reaches higher values around 25 s corresponding to an excitation frequency around 1 Hz. This occurs later for the vertical inertial sensor implying resonance at higher frequency. The amplitude of the horizontal motion is roughly an order of magnitude greater than that of the vertical motion, 10^{-2} μm versus 10^{-3} μm. Regarding angular velocities amplitude, they are similar with an order of magnitude of 10^{-2} μm, though smaller at low frequency for the vertical motion.

Again, the state observer seems to accurately represent the states of the inertial sensors. Their estimation error are plotted in Fig. 34.

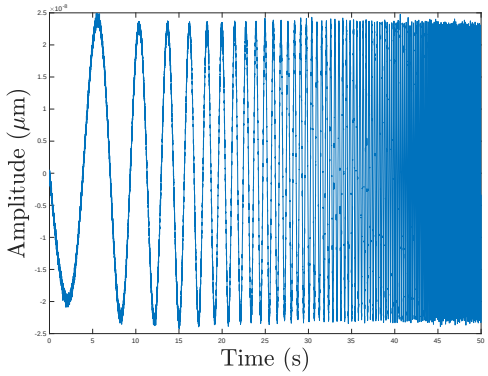

(a) θ_{H1}

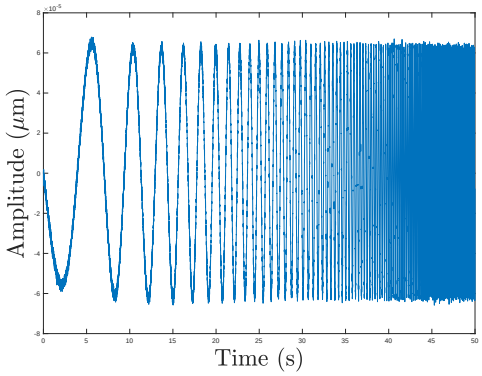

(b) ω_{H1}

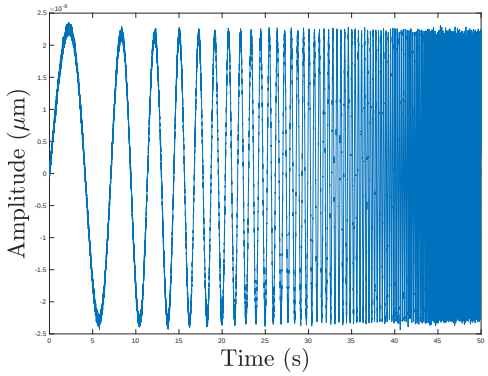

(c) θ_{V1}

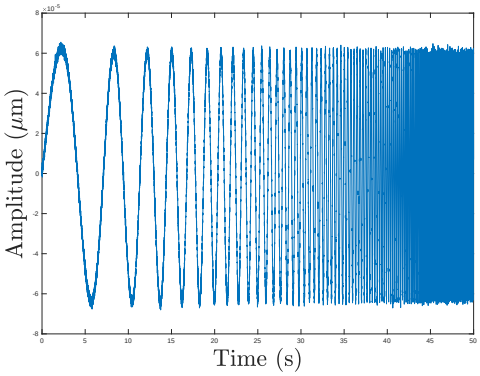

(d) ω_{V1}

Figure 34: Error between the inertial sensors' actual states and their estimates for the time response illustrated in Fig. 33.

Angle estimations of both horizontal and vertical inertial sensors have an accuracy of 10^{-8} with respect to the input disturbance while angular velocity estimations reach 10^{-5}. This time, the amplitude of the error is constant during the whole excitation duration so for the whole range of frequency. Once more, these values can be put into perspective of the motion amplitude of their respective state in order to assess the representation

accuracy of the estimations depending on the excitation frequency. It can be concluded that the representation accuracy of the angle of both sensors is roughly similar at low and high frequency and amounts to 10^{-6} %. Whereas for their angular velocity, the accuracy estimation equals 1 % at low frequency and 0.1 % at high frequency.

A table showing the error amplitude and estimation accuracy of all the inertial sensors states is given in Tab. 2. The angular velocity states are again separated into a low and high frequency domain while it is not the case for the sensors' angle state as the values were the same for the whole frequency range. The angle states of the sensors are very well estimated as their error order is of 10^{-11} with an accuracy of at least 10^{-4}% for the whole control bandwidth. The error of the angular velocity states is also of the same order for each sensors along the whole frequency range and is worth 10^{-5}. For low frequency excitation, the estimation of the angular velocity of the third vertical sensor is the worst of them with only 10 % of accuracy. The others are all around 1 % or better. The accuracy of these estimations is around 10 times better for high frequency excitation.

	θ_{H1}	θ_{H2}	θ_{H3}	θ_{V1}	θ_{V2}	θ_{V3}
Error (m)	1e-8	1e-8	1e-8	1e-8	1e-8	1e-8
Accuracy (%)	1e-6	1e-6	1e-6	1e-5	1e-5	1e-4

	ω_{H1}		ω_{H2}		ω_{H3}		ω_{V1}		ω_{V2}		ω_{V3}	
	LF	HF	LF	HF	LF	HF	LF	HF	LF	HF	LF	HF
Error (m)	1e-6		1e-5		1e-5		1e-5		1e-5		1e-5	
Accuracy (%)	1	0.1	0.1	1e-2	1	1e-2	1	0.1	1	0.1	10	0.1

Table 2: Estimation error and representation accuracy of all the inertial sensors' states of the isolation platform when subjected to a sine disturbance logarithmically swept between 0.1 Hz and 10 Hz and with an amplitude of 1 μm

5.2.3 Conclusion

To summarise, the observer is able to estimate the twenty-four states of the system with an accuracy of 0.1 % or better for an excitation frequency above 1 Hz. Regarding the sub-Hz frequency range, the observer manages to estimate most of the system's states with an accuracy of at least 1 %. The exceptions are the position of the hexagonal table in the x-direction and the angular velocity of one of the vertical sensor. They are only estimated with a 10 % accuracy which will inevitably affect the controller's performances.

5.3 LQR and LQG regulator

As mentioned in Sec 3.6, the separation principle allows to split the design of a linear quadratic Gaussian controller in two distinct parts. The first is the development of a state observer which has been done in the previous section. The second is to design

a linear quadratic regulator that will use the estimated states as if they were the real states in order to construct the feedback vector. The LQR design will now be discussed as well as the performance goal of this controller. The LQR design problem is to find the LQR gain matrix K of the feedback law (Eq. 30) that minimises the quadratic cost function J_{LQR} of Eq. 29. This is done by the *matlab* function *lqr* which takes as input the A and B state matrices representing the system and the weighting matrices Q_{LQR} and R_{LQR}. The latter must thus be addressed beforehand. Q_{LQR} has been chosen as the identity matrix so that all the states were given the same degree of importance. Matrix R_{LQR} has then been tuned to increase the controller's gain K by decreasing its entry values compared to Q_{LQR}. Higher gain values lead to more control power and thus better isolation performances. However, there are limitations to the magnitude of the gain. Indeed, as it will be seen in Sec. 5.5, sensor noise is a function of the controller gain. As a result, it is amplified as the gain is increased. The latter must then be limited to still be capable of measuring and controlling the ground motion. The parameters have been chosen to yield the highest order of isolation while keeping a relatively low sensor noise. Furthermore, the performance of the LQG controller is limited by that of the observer. Therefore, above a certain LQR gain value, increasing it does not lead to significant performance improvement of the LQG controller. Having knowledge of all these issues, the weighting matrices that have finally been chosen are

$$Q_{LQR} = \mathbb{I}_{24\times 24}, \tag{66}$$

$$R_{LQR} = 10^{-10} * \mathrm{diag}\begin{bmatrix} 0.5 & 1 & 0.5 & 1 & 0.5 & 1 \end{bmatrix}. \tag{67}$$

The values of matrix R_{LQR} have been chosen to reach roughly the same order of isolation for the diagonal terms of the transfer function matrix i.e. the six transfer functions between each actuator and its corresponding inertial sensor. The values corresponding to the horizontal pairs of actuator-sensor are lower since the horizontal isolation performances achieved by the initial plant is not as good as the vertical one. Once the LQR gain is computed, the proportional feedback law is used to close the system's loop. It should also be noted that the LQR controller designed here does not take into account the dynamic of the system outside the control bandwidth i.e. [0.1,10] Hz. Thus, it does not contain a band pass filter. The latter will be developed later on. To illustrate the isolation performances achieved by this LQR controller, the bode magnitude plots of the transfer function from H1 to HINS1 and V1 to VINS1 of both the open and closed-loop systems for comparison are shown in Fig. 35. The transfer functions for the remaining horizontal and vertical actuator-sensor pair are similar. The curve representing the closed-loop system with the LQR controller (sys_{LQR}) is seen to be below and smoother than the open-loop one. The smoothness of the curve means that the resonances of the initial system are well-damped while its decrease in magnitude indicates the isolation achieved

by the active system. Indeed, this means that ground motion disturbances, which translates into perturbations of the actuator's input, are less transferred to the inertial sensor and hence to the payload that would be placed on the hexagonal table. The closed-loop system achieves about two additional orders of isolation compared to the open-loop one in the control bandwidth. This means that the response of the system to disturbances, for instance originating from seismic vibration, will roughly be a hundred times smaller than without active control. Moreover, the magnitude of the two closed-loop transfer functions do not exceed a magnitude of 10^{-6} across the whole frequency bandwidth. This represents the overall isolation performance of the closed-loop system.

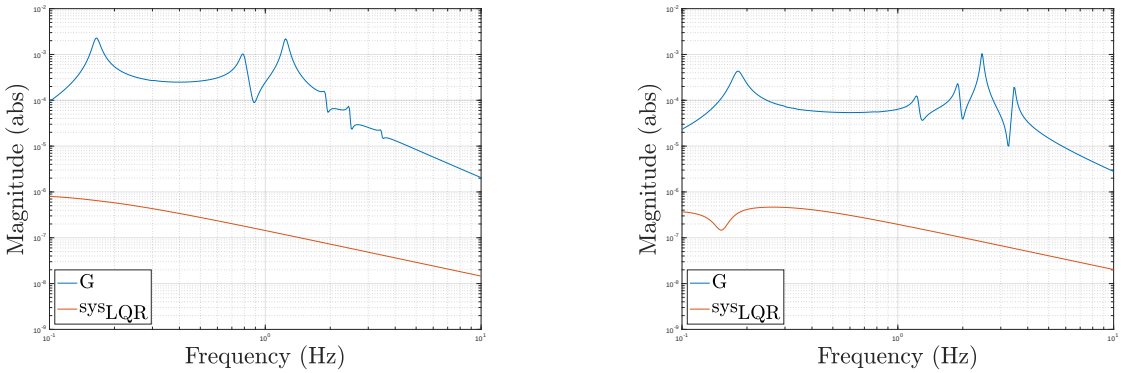

(a) H1 to HINS1 (b) V1 to VINS 1

Figure 35: Bode magnitude plots of the system's transfer function from actuator H1 to inertial sensor HINS1 and from actuator V1 to inertial sensor VINS1. Both the open-loop plant (G) and closed-loop system with LQR (sys_{LQR}) are presented for comparison.

As discussed earlier, the off-diagonal elements of the transfer function matrix must also be considered to assess the real performances of the controller. Only the coupling terms between actuator H1 and the inertial sensors VINS1 and HINS2 and VINS2 are discussed since they are representative of all of them. The magnitude of their transfer function in the control bandwidth are shown in Fig. 36. Again, the controller damps and isolate the plant but two orders of isolation is not achieved across the whole frequency range. Indeed, for the transfer function from H1 to VINS2, the relative isolation order is low. However, since the magnitude of this transfer function is initially very low at theses frequencies, the overall isolation achieved is also well below 10^{-6}. This order of isolation has been verified to be achieved for all the 36 transfer functions of the system. This number can then be roughly taken as the order of isolation the active platform with LQR control is able to produce.

Now, the K matrix defined by the LQR design can be combined with the Kalman filter for state estimation to yield an optimal LQG regulator for the plant. This is carried out

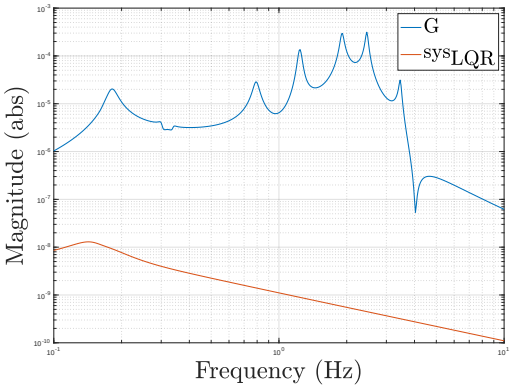

(a) H1 to VINS1

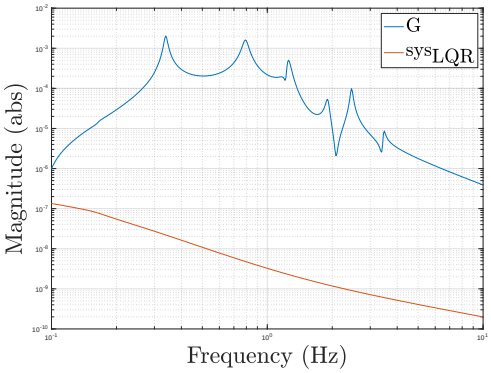

(b) H1 to HINS2

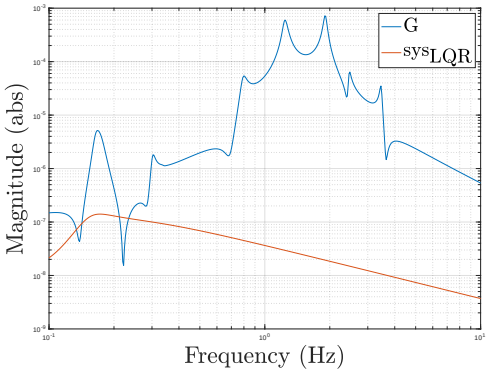

(c) H1 to VINS2

Figure 36: Bode magnitude plots of the system's transfer function from actuator H1 to inertial sensor VINS1, HINS2 and VINS2. Both the open-loop plant (G) and closed-loop system with LQR (sys_{LQR}) are presented for comparison.

by the *lqgreg* command on *Matlab*. This regulator is then used as feedback in a closed-loop system. The results and performances of this closed-loop system with LQG control are discussed in Sec. 6 after the implementation of a band-pass filter.

5.4 Band pass filter

As it has already been said, the control bandwidth is $[0.1 - 1]$ Hz. The controller is thus developed to control the plant in this frequency band and might not be appropriate outside of it. Hence, to avoid any unwanted motion amplification at frequencies outside the control bandwidth, both a low-pass and high-pass filter have been applied to the sensors used for the feedback control. The reasons for the limitations at high and low frequencies are discussed below.

5.4.1 Low pass filter

In fig 37, the amplitude of the transfer function from the first horizontal actuator (H1) to its corresponding horizontal inertial sensor (HINS 1) obtained from the experiment with a high frequency excitation is presented.

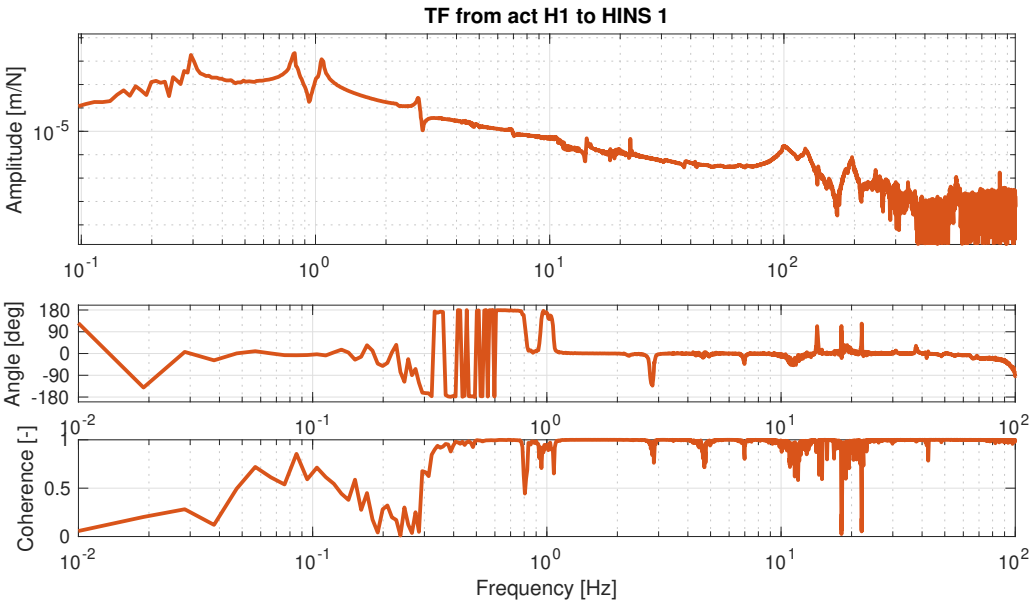

Figure 37: Experimental result of the amplitude of the transfer function from the first horizontal actuator (H1) to its corresponding horizontal inertial sensor (HINS 1).

The peaks corresponding to the resonances of the inertial sensor and to the suspension modes of the isolator already discussed may again be seen. Though, additional resonances are present. For instance, around 3 Hz, the peak corresponds to the resonance frequency of the suspension modes of the passive stage below the isolators that is not represented in the platform's model employed. Above 100 Hz, the resonance frequencies of the internal flexible modes appear. These are high frequency vibration modes that introduce a deformation of the body. High control gains should not be applied at these frequencies because stability is not assured. It would therefore excite these modes and amplify the motion of the platform. To make vibration isolation possible in the control bandwidth, the platform has been designed to have all its internal modes outside of it.As a result, a low pass filter must be applied to the sensors to reduce the control gain at high frequency and not excite the flexible modes. To this end, the following second order low-pass filter has been applied

$$\mathrm{L_P} = \frac{(2\pi \cdot 30)^2}{s^2 + 2\pi \cdot \frac{5}{4} \cdot 30 \cdot s + (2\pi \cdot 30)^2} \tag{68}$$

with $w_0 = 30$ Hz, the characteristic frequency, and $Q_p = 5/4$, the quality factor which determines the sharpness of the frequency response curve around the characteristic frequency. It provides a cut-off frequency (w_c) around 30 Hz and allows to drastically reduce

the control gain above 100 Hz.

Different methods exist to be able to control the flexible modes at high frequencies. For example, notches can be used to remove the flexible modes from the transfer function, actuators can be added to actively control them, or virtual sensor fusion technique can be applied. Though, none of them will be implemented in this thesis as the focus is on low frequency isolation.

5.4.2 High pass filter

In the low frequency band, the limitation comes from the sensors. The inertial sensors resolution, discussed in [33], is greatly reduced below 0.1 Hz. As the excitation's frequency decreases, they become less sensitive and can therefore not properly capture the motion of the platform. In this case, controlling the motion at these frequencies is impossible. As a result, a second order high-pass filter described by Eq. 69 has been applied to reduce the control gain at low frequency

$$\mathrm{H_P} = \frac{s^2}{s^2 + 2\pi \cdot \frac{5}{4} \cdot 0.05 \cdot s + (2\pi \cdot 0.05)^2} \tag{69}$$

with $w_0 = 0.05$ Hz and $Q_p = 5/4$. It provides a cut-off frequency around 0.05 Hz.

5.4.3 Band pass filter

Together, the low and high-pass filter form the band-pass filter shown in Fig 38. The low and high-pass filters are also represented.

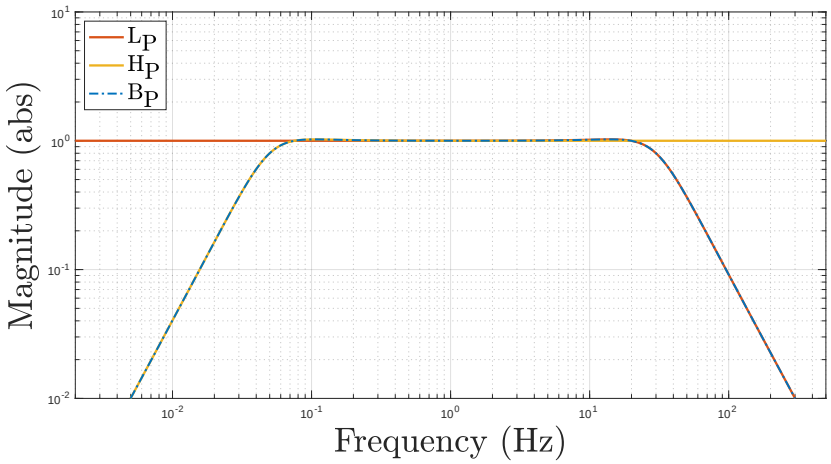

Figure 38: Band-pass filter implemented in the control loop. $\mathrm{L_P}$ is the low-pass filter, $\mathrm{H_P}$ is the high-pass filter, and $\mathrm{B_P} = \mathrm{L_P} \cdot \mathrm{H_P}$ is the band-pass filter.

The filter equals unity in the control bandwidth and drops at a rate of two orders of

magnitude per decade of frequency at low and high frequency. It may be seen that by the time it reaches the 100 Hz frequency value, its magnitude has already dropped by ten. The 3-db line defines the frequency at which the power of the signal is reduced by half of its maximum value. It is often used to define the frequency bandwidth of the filter. In absolute units, it corresponds to the frequency at which the signal amplitude equals 0.707 times its maximum amplitude. Using this convention, the cut-off frequencies of the high and low pass filters are 0.009 Hz and 33 Hz respectively. The frequency bandwidth of the filter is thus [0.045-33] Hz. The band-pass filter is then implemented in the control loop to limit the controller to the filter bandwidth.

5.5 Noise budget

In practice, noise sources present within the active isolation system limit its performances. They each impact the system in ways and frequencies that are specific to them. To identify the limitations introduced by the different noise sources and at which frequencies they appear, a noise budget is performed. They are many sources of noise but only the main ones have been studied. The noise taken into account are the sensor noise (n_{s}), coming from the limited resolution of the inertial sensors, the noise introduced by the current injector (n_{ci}) responsible for amplifying the current between the controller and the actuators, and finally the ground motion itself (w). With these noises sources in the feedback loop, the force applied by the actuator on the hexagonal table is expressed as

$$f = n_{ci} - H(x + n_s). \tag{70}$$

Introducing this expression in Eq. (6) describing the dynamic of the active platform, it becomes

$$ms^2X + cs(X - W) + k(X - W) = n_{ci} - H(x + n_s). \tag{71}$$

Isolating the payload's motion X on the left hand side of the equation, the following equation is obtained

$$X = \frac{k + cs}{H + ms^2 + cs + k}W + \frac{H}{H + ms^2 + cs + k}N_c + \frac{1}{H + ms^2 + cs + k}N_{ci}. \tag{72}$$

Assuming that the three noise sources are uncorrelated, the power spectral density (PSD) of X can be written as

$$\phi_x = \Big|\frac{k + cs}{H + ms^2 + cs + k}\Big|^2\phi_w + \Big|\frac{H}{H + ms^2 + cs + k}\Big|^2\phi_s + \Big|\frac{1}{H + ms^2 + cs + k}\Big|^2\phi_{N_{ci}} \tag{73}$$

where ϕ_w, ϕ_s, $\phi_{N_{ci}}$ are the PSDs of the ground motion, the sensor noise, and the current injector noise respectively. These PSDs are then compared to see what is the source of

the residual motion of the platform at each frequency. Both an horizontal and vertical noise budget analysis has been performed since the parameters of the platform and the noise sources differ for the two components. The noise budget for the horizontal motion is shown in Fig. 39. The platform's parameters used for the horizontal noise budget are the following

$$\begin{aligned} m &= 250 \text{ kg}, \\ k &= 8125 \text{ N/m}, \\ c &= 70 \text{ N/m/s}. \end{aligned} \tag{74}$$

The PSD of the ground motion has been obtained from measurements at the *Centre Spatial de Liège* close to the university where the isolation platform is stored. The one of the current injector is an inherent characteristic of the machine. And finally the PSD of the sensor noise is based on the inertial sensor resolution developed in [33]. As the sensor noise data were not available, a similar curve has been computed to resemble the results from the thesis. This curve is actually an upper bound of the real one to simply show that the controller is not limited by sensor noise in the control bandwidth.

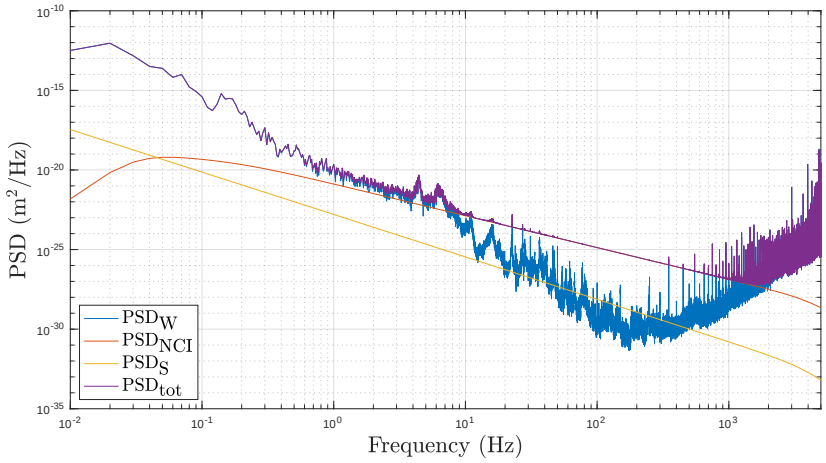

Figure 39: Horizontal noise budget of the isolation platform. The PSD of the residual motion of the platform, noted PSD_{tot} is obtained from the addition of the PSDs of the ground (PSD_{W}), the current injector noise (PSD_{NCI}) and the sensor noise (PSD_{S}).

The graph shows that the PSD of the payload's motion is dominated by the ground motion up to 10 Hz and from 10^3 Hz and above. In between, the current injector noise dictates the payload's motion. This implies that the active platform augmented with the controller designed is not limited by the system's noises in the control bandwidth.
The similar analysis is done for the vertical motion. The platform's vertical parameters are

$$\begin{aligned} m &= 250 \text{ kg}, \\ k &= 0.33e5 \text{ N/m}, \\ c &= 45 \text{ N/m/s}. \end{aligned} \tag{75}$$

The vertical noise budget is plotted in Fig. 40. The results are similar to the horizontal noise budget apart from the fact that the sensor noise is dominant below 0.04 Hz. Fortunately, this is not in the control bandwidth. The analysis again shows that the system's noises are sufficiently low in the control bandwidth for the active system to work efficiently.

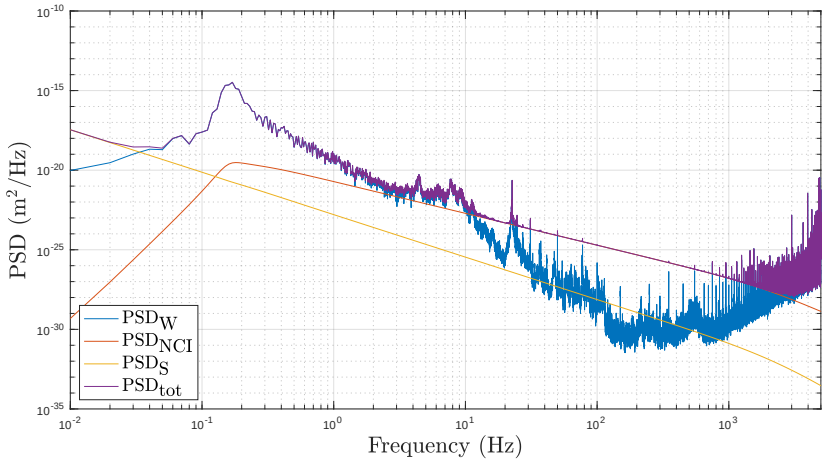

Figure 40: Vertical noise budget of the isolation platform. The PSD of the residual motion of the platform, noted $\mathrm{PSD_{tot}}$ is obtained from the addition of the PSDs of the ground ($\mathrm{PSD_W}$), the current injector noise ($\mathrm{PSD_{NCI}}$) and the sensor noise ($\mathrm{PSD_S}$)

The PSD of the actuator force may also be computed. It is given by

$$\phi_f = H^2 \phi_x + \phi_{N_{ci}}. \tag{76}$$

An interesting quantity to investigate is its cumulative root mean square (R.M.S) value. It gives a measure of the average energy in the signal. So in the case of a force, it informs about the force that the actuators need to apply to effectively isolate the platform from ground motion. From the transducer constant of the actuators, this value, in units of N^2, can be transformed in a value in A^2. The latter hence gives an estimation of the current that will need to be supplied to the actuators to allow them to develop the appropriate control force. If the system is not able to provide a strong enough current, the actuators will apply a weaker force than needed to cancel the platform's motion. As a result, the active isolation of the platform would not work. The R.M.S values of the amplitude spectral density (ASD) of the horizontal and vertical actuator force, are plotted in Fig. 41. The ASDs have been used to have a value in ampere as they are basically the square root of the PSDs. It shows that the greater control inputs are needed at low frequency than high frequency. Moreover, the vertical actuators require a stronger current than the horizontal one. This is partly due to the higher horizontal actuator constant meaning that the horizontal actuators can develop a stronger force with same input current. In any case, the R.M.S values of both actuators do not exceed 20 mA. Considering that the

current amplifier can output a current of up to 1 A, it can be concluded that the existing components of the system are suitable for the active isolation platform.

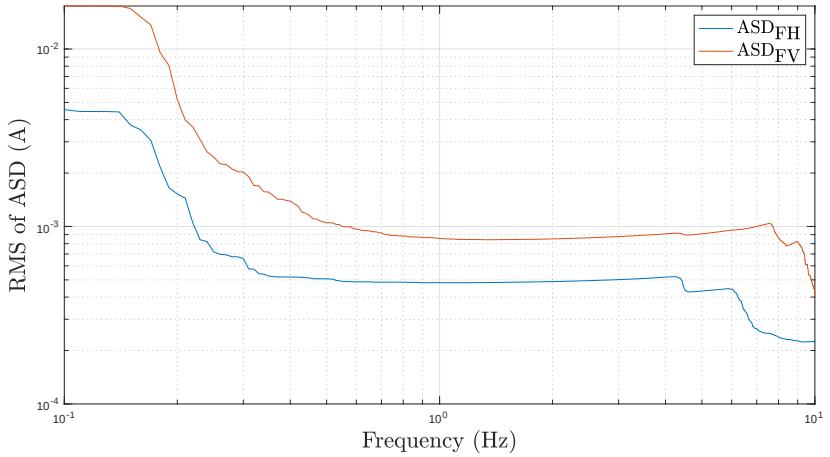

Figure 41: R.M.S values of the amplitude spectral density (ASD) of the horizontal and vertical actuator force.

6 Tests and results

The complete LQG controller designed in Sec. 5 is finally implemented as feedback to the open-loop plant. The isolation performances of the resulting closed-loop system are discussed in this section. First, Bode magnitude plot comparing the system with control-off and control-on are presented. Then, the time response of both systems to an input disturbance simulating ground motion due to seismic activity are analysed. A general conclusion of the result is finally provided.

In Fig. 42, the Bode magnitude plots of the transfer function from actuator H1 to the inertial sensor HINS1 as well as from actuator V1 to the inertial sensor VINS1 are shown.

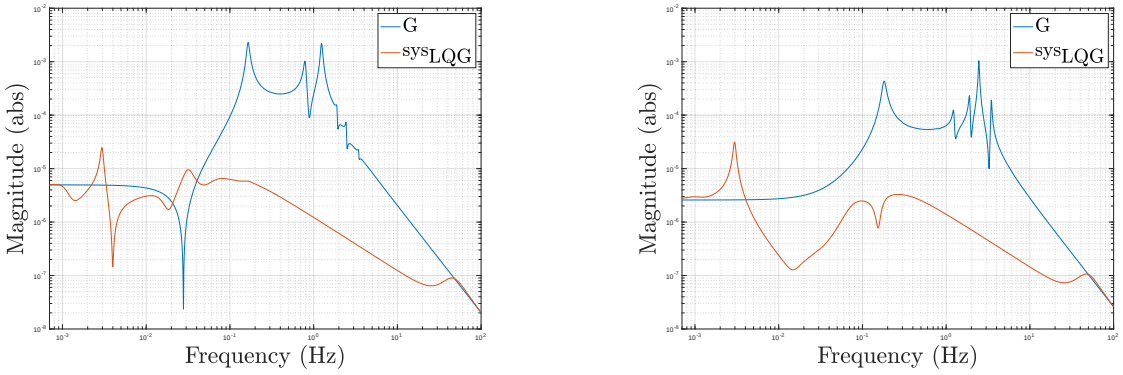

(a) H1 to HINS1 (b) V1 to VINS1

Figure 42: Bode magnitude plots of the system's transfer function from actuator H1 to inertial sensor HINS1 and from actuator V1 to inertial sensor VINS1. Both the open-loop plant (G) and closed-loop system with LQG (sys_{LQG}) are presented for comparison.

The first one is representative of the interaction of the three horizontal actuator-sensor pairs. And the second one illustrates the interaction of the three vertical actuator-sensor pairs. The resonances of the different elements constituting the platform are seen to be well damped. Moreover, the magnitude of the closed-loop transfer functions are seen to be at least one order of magnitude lower than the initial plant's ones across the whole control bandwidth. Outside of it, the effects of the band pass filter may be seen. At high frequency, the controller gain is seen to be reduced around 30 Hz and reaches zero around 50 Hz. However, at low frequency, the controller is not quickly and smoothly decreased. Indeed, at the crossover frequency of the high pass filter, around 0.05 Hz, the closed-loop transfer function curve follows a path a bit erratic before meeting the open-loop one. It creates sharp peaks between 10^{-2} Hz and 10^{-3} Hz that is likely due to a bad phase margin at these frequencies. The controller parameters probably needs a bit more tuning to attenuate this effect. The overall isolation in the high part of the frequency bandwidth (from 1 Hz to 10 Hz)) of both the horizontal and vertical components is sim-

ilar and is comprised between 10^{-6} and 10^{-7}. Their performances decrease in the low frequency part (from 0.1 Hz to 1 Hz) especially for the horizontal components. Though, both have a magnitude below 10^{-5} in the whole frequency bandwidth and this is true for the four other diagonal elements of H. This implies that an initial perturbation imposed to the platform could be decreased by approximately five orders of magnitude whereas the control-off plant could only achieve about two or three.

The same off-diagonal elements of H discussed in Sec. 5.3 are shown in Fig. 43.

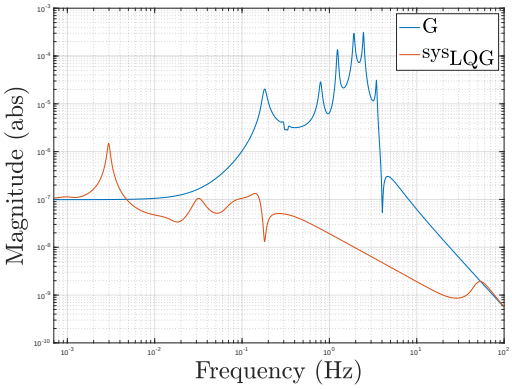

(a) H1 to VINS1

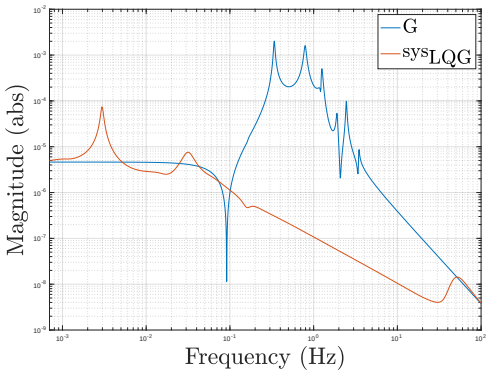

(b) H1 to HINS2

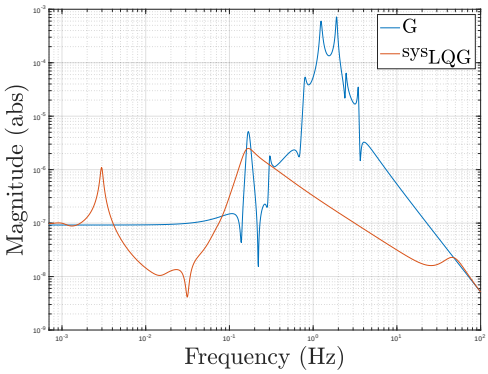

(c) H1 to VINS2

Figure 43: Bode magnitude plots of the system's transfer function from actuator H1 to inertial sensor VINS1, HINS2 and VINS2. Both the open-loop plant (G) and closed-loop system with LQG (sys_{LQG}) are presented for comparison.

They are the transfer functions from H1 to VINS1, HINS2 and VINS2. The coupling term that exhibits the worst performances is the one between H1 and VINS2. Indeed, below 0.3 Hz, the controller doesn't improve the isolation of the initial plant. Though, the magnitude still remains below 10^{-5} so that it does not affect the performances achieved with the diagonal terms. As before, the isolation increases with the excitation frequency and reach 10^{-6}. For the two other transfer functions, the magnitude of the closed-loop

system is below 10^{-6} at low frequency and 10^{-7} at high frequency. The magnitude curve of the controlled system is verified to be lower than 10^{-5} below 1 Hz and than 10^{-6} above it for all the thirty-six transfer functions of the system.

To illustrate the isolation achieved by the active system, the same disturbance with a frequency swept across the control bandwidth used in Sec. 5.2 is applied to the actuator inputs to simulate ground motion. The graphs plotted in Fig. 44 are the time response of the first horizontal inertial sensor obtained by applying the disturbance to its corresponding horizontal actuator (H1). The response of the open-loop plant shows to have an amplitude around the order of 10^{-4} and up to 10^{-3} around 30 s. This time corresponds to the resonance of the isolator's suspension mode between 1 Hz and 2 Hz. The response of the closed-loop system is plotted separately for clarity. Its shape is significantly different than the open-loop. Indeed, no resonances are to be seen around 1 Hz as these suspension modes have been completely damped. Instead, the response's maximum amplitude occurs at the beginning of the excitation, hence at low frequency. It then decreases exponentially with the excitation's frequency. The amplitude peaks around $8 \cdot 10^{-6}$ and decreases to 10^{-7} after 35 s.

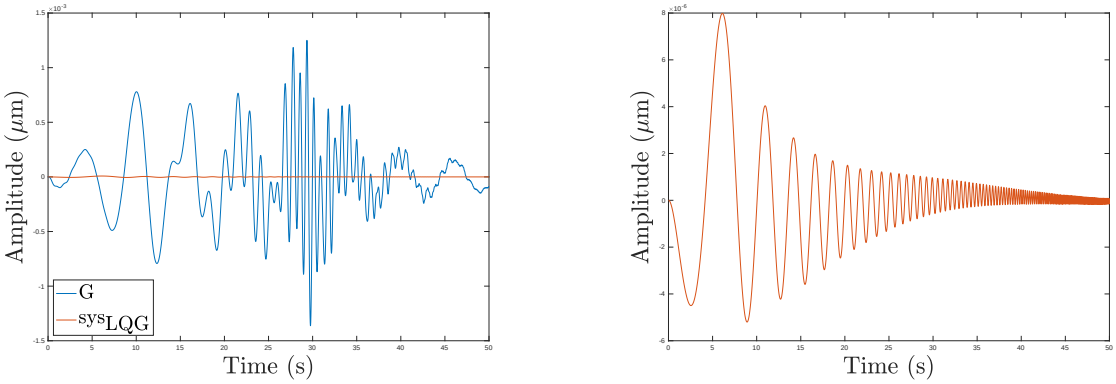

(a) Control-off and control-on systems' responses

(b) Close up on the control-on system's response

Figure 44: Time response of HINS1 to a sine disturbance logarithmically swept between 0.1 Hz and 10 Hz and with an amplitude of 1 μm applied to actuator H1. The control-off (G) and control-on (sys_{LQG}) systems are compared.

The same disturbance has been applied to the first vertical actuator V1 and the response of its corresponding vertical inertial sensor output is displayed in Fig. 45. The open-loop response is overall smaller than the horizontal response was when exciting its related actuator. The amplitude is of the order of 10^{-4} with a peak around $3 \cdot 10^{-4}$ appearing between 35 s and 40 s. This one corresponds to the vertical suspension modes of the isolator. The amplitude of the vertical inertial sensor's response in closed-loop is unsurprisingly lower than that of the horizontal sensor. Again, it is greater at low frequency, with an amplitude of 10^{-6}, and drops to 10^{-7} at high frequency.

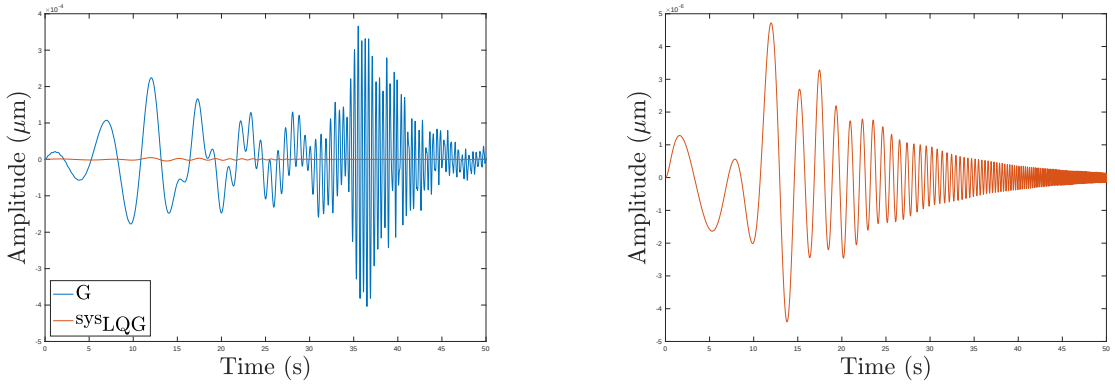

(a) Control-off and control-on systems' responses (b) Close up on the control-on system's response

Figure 45: Time response of VINS1 to a sine disturbance logarithmically swept between 0.1 Hz and 10 Hz and with an amplitude of 1 μm applied to actuator V1. The control-off (G) and control-on (sys_{LQG}) systems are compared.

An actual ground motion disturbance impacts all the actuators instead of only one. Hence, in order to address the performances of the active platform to ground motion-like perturbations, the swept sine signal is now applied to all the six actuators of the system. The time response of the outputs measured by the inertial sensors are then studied. On Fig. 46, the response of the three horizontal inertial sensors of the system with control-off and control-on are compared.

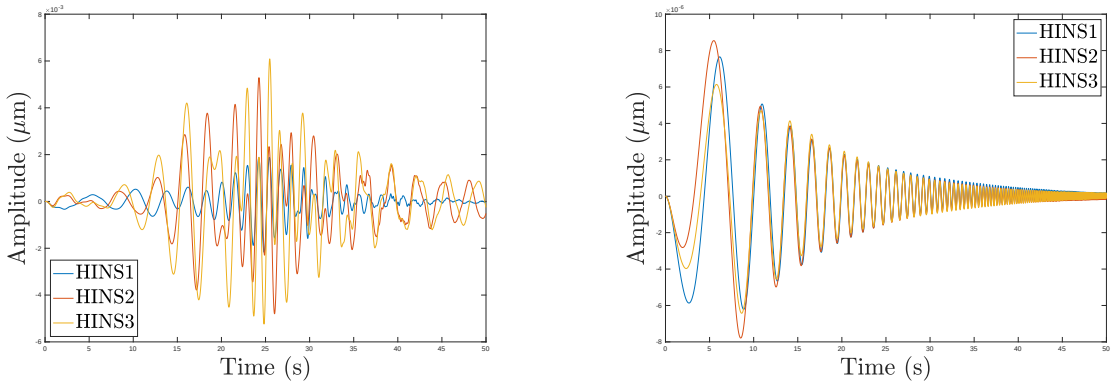

(a) Control-off and control-on systems' responses (b) Close up on the control-on system's response

Figure 46: Time response of the three horizontal inertial sensors to a sine disturbance logarithmically swept between 0.1 Hz and 10 Hz and with an amplitude of 1 μm applied to the six actuators. The control-off (G) and control-on (sys_{LQG}) systems are compared.

The results are very similar than when only one actuator is excited. The resonances of the isolator's suspension are still seen to occur around 1 Hz for the uncontrolled plant. Though, it can be noticed that HINS2 and HINS3 have an amplitude of motion greater by a factor 2 to 3 than HINS1. The motion amplitude is nevertheless bounded below 10^{-2} μm and decreases to 10^{-3} μm at the very ends of the control bandwidth. Despite

the amplitude difference between the three sensors for the open-loop system, their motion when in closed-loop are almost identical. They are the greatest at low frequency with an amplitude order of 10^{-7} μm and rapidly decreases to 10^{-8} μm at high frequency.

Regarding the motion in the vertical direction, the time response of the three vertical inertial sensors are shown in Fig. 47. Similarly to Fig. 45(a), the response's amplitude does not exceed 10^{-3} m with a peak around the resonance frequencies of the isolators' vertical suspension modes. It is also the third sensor, VINS3, that exhibits the highest amplitude at resonances whereas it is the opposite at low frequency. When the control of the system is turned on, the three vertical sensors are subjected to the same motion which is again higher at low frequency and gradually decreasing as the latter is increased. The amplitude of their overall motion is limited below $8 \cdot 10^{-6}$, just like the horizontal inertial sensors.

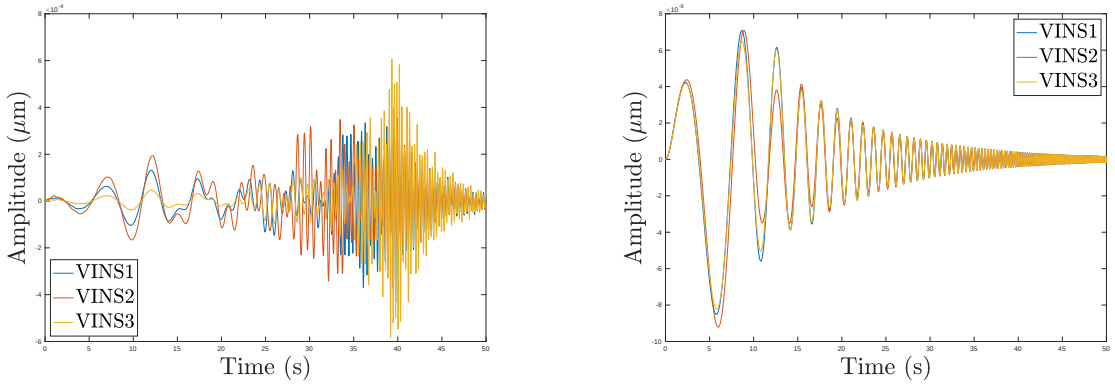

(a) Control-off and control-on systems' responses

(b) Close up on the control-on system's response

Figure 47: Time response of the three vertical inertial sensors to a sine disturbance logarithmically swept between 0.1 Hz and 10 Hz and with an amplitude of 1 μm applied to the six actuators. The control-off (G) and control-on (sys_{LQG}) systems are compared.

To summarise, the controller allows to effectively decrease the horizontal and vertical motion of the platform. And it decreases both motion to the same amplitude even though the initial amplitude in the vertical direction is lower. Moreover, it is more efficient at high frequency than low frequency. Indeed, the orders of magnitude of isolation achieved are about one between 0.1 Hz and 1 Hz and two from 1 Hz to 10 Hz.

7 Conclusion and future work

This last chapter presents first the final conclusion and then possible future work that could be carried out to improve what has been developed in this thesis.

7.1 Conclusion

The objective of this work was to design a type of optimal controller, called a linear quadratic Gaussian (LQG), for an existing hybrid isolation platform. To achieve this, methods for passive and active isolation have first been reviewed. Then the theoretical basis related to the active control of systems have been laid out. The concepts of transfer function, linear quadratic regulator, state observer and Kalman filter were explained.

Next, the existing experimental platform for which the controller is designed have been introduced. Some of its important components as the inertial sensors, the current amplifier and the isolators have been further discussed. Afterwards, the plant's model corresponding to the experimental platform to be used for the control design has been described. Some of its important features for controller design has been discussed. These are its stability, observability, and controllability. The last two guarantees the possibility to develop this LQG controller. Some of its transfer function were also presented to learn about its dynamic in open-loop.

Once all the tools to develop the controller were in hand, the design begun. As the plant's state cannot be measured directly, the first step was to design a state observer to reconstruct its states from the sensors' outputs. This has been done with the help of a Kalman filter which takes into account the measurement and process noise present in the system assuming they have a Gaussian distribution with zero mean. Analysis performed on the observer showed that it was able to estimate the system's states with an accuracy of 0.1 % when the plant is excited at frequencies above 1 H. However its performances are reduced in the low frequency part of the control bandwidth i.e. from 0.1 Hz to 1 Hz, where it only has an accuracy of about 1 % for most of the states and drops to 10 % for a couple of them.

The second step is the LQR gain computation. The LQR is another type of optimal controller which assumes perfect knowledge of all the system's sates. That doesn't happen in real life application but when used with a state observer, it can achieve good control performances. Bode plots picturing the performances of this controller were showed to give insights on the possible performances of the LQG. The overall order of isolation achieved by the LQR was 10^{-6} at low frequency and 10^{-7} at high frequency.

The state observer and LQR gain were then combined to form an LQG regulator to use as

feedback in the control loop. In addition, a band pass filter to prevent the controller from acting at frequencies for which it is not appropriate has been designed and implemented in the loop. Finally a noise budgeting of the various noise sources present within the system has been performed.

At last, the performances of the closed-loop system with LQG has been investigated. To this end, a sine disturbance swept from 0.1 Hz to 10 Hz has been applied to the six actuators to simulate ground vibration. The time response of the control-off and control-on system have then been compared. From this analysis, it emerged that the controller allows to increase the isolation performances of the platform by about one order of magnitude between 0.1 Hz and 1 Hz and by two order of magnitudes from 1 Hz to 10 Hz. Therefore, it can be concluded that this type of controller is appropriate to provide good isolation performances to the experimental platform in the control bandwidth $[0.1, 10]$ Hz.

7.2 Future work

Several improvements perspectives arise from this work. First of all, this controller should be implemented in practice to show its real experimental performances. From this study, its shortcomings can be identified and then improved. For instance, one of the problem is that the measurement noise covariance matrix of the observer has only been guessed. As a result, it does not represent the actual noise inherent to the system. It must be inferred from experimental tests on the platform. Also, the Kalman filtering techniques used assumes a Gaussian distribution of the noise, limiting the representation of the actual noises. Instead, other types of filter like the particle filter may be used to represent the noise distribution as reliably as possible. Moreover, it has been mentioned that the high pass filter introduces peaks in the transfer functions of the system between 10^{-3} and 10^{-2} Hz likely due to a poor phase margin at these frequencies. The parameters of the controller can be tuned to attenuate this effect.

References

[1] J-M. Gérard. *Relativité générale*. University lecture notes. Université catholique de Louvain, 2018.

[2] Energy Wave Theory project. *Spacetime*. URL: https://energywavetheory.com/spacetime/. (accessed: 11.05.2022).

[3] J-M. Gérard. *Relativité restreinte*. University lecture notes. Université catholique de Louvain, 2017.

[4] LIGO Caltech. *Sources and Types of Gravitational Waves*. URL: https://www.ligo.caltech.edu/page/gw-sources. (accessed: 05.04.2022).

[5] A. Le Tiec and J. Novak. "Theory of Gravitational Waves". In: (July 2016).

[6] D. N. Spergel. "The Cosmic Microwave Background A Gravity Wave Detector". In: *AIP Conference Proceedings* 575.1 (2001). DOI: https://doi.org/10.1063/1.1387312.

[7] V. Gladyshev and I. Fomin. *The Early Universe as a Source of Gravitational Waves*. IntechOpen, 2019. DOI: 10.5772/intechopen.87946.

[8] M. Maiorano, F. De Paolis, and A. A. Nucita. "Principles of Gravitational-Wave Detection with Pulsar Timing Arrays". In: *Symmetry* 13.12 (2021). DOI: https://doi.org/10.3390/sym13122418.

[9] NASA Goddard Space Flight Center. *Gravitational Astrophysics Research*. URL: https://science.gsfc.nasa.gov/663/research/index.html. (accessed: 10.05.2022).

[10] C. Bond et al. "Interferometer techniques for gravitational-wave detection". In: *Living Rev Relativ* 19.3 (2016). DOI: https://doi.org/10.1007/s41114-016-0002-8.

[11] P Hariharan. *Basics of interferometry*. second edition. Elsevier, 2007. ISBN: 978-0-12-373589-8.

[12] M. G. Beker. "Low-frequency sensitivity of next generation gravitational wave detectors". PhD thesis. Vrije Universiteit Amsterdam, 2013.

[13] C-M. Chen, J. M. Nester, and W-T. Ni. "A brief history of gravitational wave research". In: (2016). DOI: https://doi.org/10.48550/arXiv.1610.08803.

[14] F. Acernese et al. "Measurements of Superattenuator seismic isolation by Virgo interferometer". In: *Classical and Quantum Gravity* 33.3 (2010), pp. 182–189. DOI: https://doi.org/10.1016/j.astropartphys.2010.01.006.

[15] F. Acernese et al. "Advanced Virgo: a second-generation interferometric gravitational wave detector". In: *Classical and Quantum Gravity* 32.2 (2015), p. 52. DOI: 10.1088/0264-9381/32/2/024001.

[16] J. Casanueva Diaz. “Control of the gravitational wave interferometric detector Advanced Virgo”. PhD thesis. Université Paris-Saclay, 2017.

[17] D. Bersanetti et al. “Advanced Virgo: Status of the Detector, Latest Results and Future Prospects”. In: *Universe* 7.322 (2021). DOI: https://doi.org/10.3390/universe7090322.

[18] G. Losurdo. “Ground-based gravitational wave interferometric detectors of the first and second generation: an overview”. In: *Classical and Quantum Gravity* 29.12 (2012). DOI: 10.1088/0264-9381/29/12/124005.

[19] LIGO Caltech. *LIGO-India: A Planned Joint India-US Detector*. URL: https://www.ligo.caltech.edu/page/ligo-india. (accessed: 24.04.2022).

[20] F. Matichard et al. “Seismic isolation of Advanced LIGO: Review of strategy, instrumentation and performance”. In: *Classical and Quantum Gravity* 32.18 (2015). DOI: 10.1088/0264-9381/32/18/185003.

[21] C. Affeldt et al. “Advanced techniques in GEO600”. In: *Classical and Quantum Gravity* 31.22 (2014). DOI: 10.1088/0264-9381/31/22/224002.

[22] K. L. Dooley et al. “GEO 600 and the GEO-HF upgrade program: successes and challenges”. In: *Classical and Quantum Gravity* 33.7 (2016). DOI: 10.1088/0264-9381/33/7/075009.

[23] H. Lück et al. “The upgrade of GEO 600”. In: *J. Phys.: Conf. Ser.* 228 (2010). DOI: 10.1088/1742-6596/228/1/012012.

[24] T. Akutsu et al. “Overview of KAGRA: Detector design and construction history”. In: *Progress of Theoretical and Experimental Physics* 2021.5 (2021). DOI: 10.1093/ptep/ptaa125.

[25] Y. Akiyama et al. “Vibration isolation system with a compact damping system for power recycling mirrors of KAGRA”. In: *Classical and Quantum Gravity* 36.9 (2019). DOI: https://doi.org/10.1088/1361-6382/ab0fcb.

[26] Y. Michimura et al. “Mirror actuation design for the interferometer control of the KAGRA gravitational wave telescope”. In: *Classical and Quantum Gravity* 34.22 (2017). DOI: https://doi.org/10.1088/1361-6382/aa90e3.

[27] B. Sathyaprakash et al. “Corrigendum: Scientific objectives of Einstein Telescope”. In: *Classical and Quantum Gravityy* 30.7 (2012). DOI: 10.1088/0264-9381/30/7/079501.

[28] S. Hild et al. “Sensitivity Studies for Third-Generation Gravitational Wave Observatories”. In: *General Relativity and Quantum Cosmology* 28 (2010). DOI: https://doi.org/10.48550/arXiv.1012.0908.

[29] M. Punturo et al. “The Einstein Telescope: a third-generation gravitational wave observatory”. In: *Classical and Quantum Gravityy* 27.19 (2010). DOI: 10.1088/0264-9381/27/19/194002.

[30] D. A. Shaddock. “An Overview of the Laser Interferometer Space Antenna”. In: *Publications of the Astronomical Society of Australia* 26.2 (2009), pp. 128–132. DOI: https://doi.org/10.1071/AS08059.

[31] R. T. DeRosa. “Performance of Active Vibration Isolation in the Advanced LIGO Detectors”. PhD thesis. Louisiana State University, 2014.

[32] J. Watchi. “Active seismic isolation using interferometric inertial sensors”. PhD thesis. Université de Liège, 2022.

[33] B. Ding. “Development of High Resolution Interferometric Inertial Sensors”. PhD thesis. Ecole polytechnique de Bruxelles, 2021.

[34] K Ogata. *Modern control engineering*. fifth edition. Pearson, 2009. ISBN: 0-13-615673-8.

[35] R. L. Williams II and D. A. Lawrence. *Linear state-space control system*. John Wiley and sons, inc., 2007. ISBN: 978-0-471-73555-7.

[36] H. K. Wimmer. “The Algebraic Riccati Equation: Conditions for the Existence and Uniqueness of Solutions”. In: *Linear algebra and its applications* 58 (1984), pp. 441–452. DOI: https://doi.org/10.1016/0024-3795(84)90224-6.

[37] T. Damm and C. Ethington. “Detectability, Observability, and Asymptotic Reconstructability of Positive Systems”. In: *Lecture Notes in Control and Information Sciences* 389 (1970). DOI: 10.1007/978-3-642-02894-6_6.

[38] S. G. Mohinder and P. A. Angus. *Kalman Filtering: Theory and Practice Using MATLAB*. second edition. John Wiley and sons, inc., 2001. ISBN: 0-471-26638-8.

[39] D. Alazard. *Introduction to Kalman filtering*. University lecture notes. Institut supérieur de l’aéronautique et de l’espace, 2011.

[40] MATLAB. *Nonlinear State Estimators | Understanding Kalman Filters, Part 5*. Youtube. 2017. URL: https://www.youtube.com/watch?v=Vefia3JMeHE&list=PLn8PRpmsu08pzi6EMiYnR-076Mh-q3tWr&index=5. (accessed: 12.04.2022).

[41] S. Skogestad and I. Postlethwaite. *Multivariable feedback control: analysis and design*. second edition. John Wiley and sons, inc., 2005. ISBN: 978-0-470-01167-6.

[42] T. G. Tryphon and A. Lindquist. “The Separation Principle in Stochastic Control, Redux”. In: *IEEE Transactions on Automatic Control* 58.10 (2013), pp. 2481–2494. DOI: 10.1109/TAC.2013.2259207.

[43] C. Collette et al. “Review of sensors for low frequency seismic vibration measurement”. In: (2011).

[44] H. Li, Y. Li, and J. Li. "Negative stiffness devices for vibration isolation applications: A review". In: *Advances in Structural Engineering* 23.8 (2020), pp. 1739–1755. DOI: https://doi.org/10.1177/1369433219900311.

[45] Motion control tips. *How do rotary voice coil actuators work?* URL: https://www.motioncontroltips.com/how-do-rotary-voice-coil-actuators-work/. (accessed: 29.05.2022).

[46] Q. Wu et al. "Design of a Maglev Inertial Actuator with High Mass Power Ratio for Lateral Vibration Control of Propulsion Shafting". In: *Actuators* 10.12 (2021). DOI: https://doi.org/10.3390/act10120315.

[47] The MathWorks. *MATLAB Simscape Library*. 2021. URL: https://nl.mathworks.com/products/simscape.html.